Spectrum of the Autoionizing Triplet Gerade Rydberg States of H₂ and its Analysis Using Multichannel Quantum-Defect Theory

Journal Article

Author(s):
Sprecher, Daniel; Jungen, Christian; Merkt, Frédéric

Spectrum of the autoionizing triplet *gerade* Rydberg states of H$_2$ and its analysis using multichannel quantum-defect theory

Daniel Sprecher,[†] Christian Jungen,[‡,¶] and Frédéric Merkt[*,†]

Laboratory of Physical Chemistry, ETH Zürich, 8093 Zürich, Switzerland, and Laboratoire Aimé Cotton du CNRS, Université de Paris-Sud, 91405 Orsay, France

E-mail: frederic.merkt@phys.chem.ethz.ch

---

[*]To whom correspondence should be addressed
[†]ETH Zürich
[‡]Université de Paris-Sud
[¶]Visiting Professor at ETH Zürich (2005–2006)

Abstract

A new spectrum of the autoionizing triplet states of *gerade* symmetry of H_2 has been recorded from the $v'' = 1\text{–}4, N'' = 1\text{–}3$ rovibrational levels of the metastable $c\,^3\Pi_u^-$ state in a supersonic beam. The spectrum consists of overlapping ns and nd Rydberg series with n in the range between 4 and 45 converging to the $v^+ = 1\text{–}4, N^+ = 0\text{–}5$ levels of the $X^{+\,2}\Sigma_g^+$ ground state of H_2^+. Numerous perturbations caused by s-d and rovibrational channel interactions are revealed in the spectrum and were fully assigned by combining double-resonance experiments and *ab initio* multichannel quantum-defect theory (MQDT). The energy- and internuclear-distance-dependent eigenquantum-defect parameters of MQDT were derived from available *ab initio* calculations of the low-lying electronic states of H_2 and the ground state of H_2^+ and were subsequently refined in a global fit to experimental data. The positions of 552 triplet ns and nd Rydberg levels of H_2 (361 of which were measured in the present study) could be reproduced with a root-mean-square deviation of $0.2\,\mathrm{cm}^{-1}$.

Keywords: molecular hydrogen, MQDT, rovibrational channel interaction, s-d interaction, discharge

Introduction

Because of its fundamental and astrophysical importance, the hydrogen molecule has attracted the interest of both experimentalists and theoreticians for decades. Many excited singlet and triplet states, especially those with principal quantum number $n \leq 4$ and below the $n = 2$ dissociation threshold, were first observed in emission of H_2 excited by a discharge.[1,2] Most studies of higher excited states focussed on the singlet-p manifold of *ungerade* symmetry because these states are accessible by absorption of a single vacuum-ultraviolet photon from the $X\,^1\Sigma_g^+$ ground state.[3–6] Because of couplings between electronic and nuclear motion, the Rydberg states have a strongly perturbed energy-level structure, and the dynamics of the levels located above the dissociation and ionization thresholds is complex and reveals competitive predissociation, autoionization and radiative decay processes.[7,8]

Multichannel quantum-defect theory (MQDT) has been successful in quantitatively accounting for both the structure and dynamics of these highly-excited *ungerade* states.[9,10] In the most favorable case of the $np\pi\,^1\Pi_u^-$ Rydberg series, the position of the lowest member ($n = 2$) was calculated only $0.14\,\mathrm{cm}^{-1}$ below the experimental value[11] and the positions of states around $n = 60$ could be reproduced with a root-mean-square deviation of $40\,\mathrm{kHz}$ ($\sim 10^{-6}\,\mathrm{cm}^{-1}$), after minor adjustments of the eigenquantum defects from their *ab initio* values.[12]

The treatment of *gerade* states of H_2 is more challenging because these states are characterized by strong interactions between singly and doubly-excited electronic configurations. In the singlet manifold, these interactions result, among other effects, in the well-known double-minimum potentials of the $2s\sigma\,EF$, $3s\sigma\,H\bar{H}$ and $3d\sigma\,GK$ states. Accurate *ab initio* treatments of these low-n states were achieved using the coupled-equation approach[13–15] and MQDT.[16–20] Attempts at extending the MQDT calculations to high-n *gerade* Rydberg states, for which the interaction with the doubly-excited states leads to strong predissociation, were either of moderate accuracy[21] or restricted to only a small part of the spectrum.[22]

A few years ago, millimeter-wave transitions between Rydberg states of ortho-H_2 around $n = 60$ were observed in our laboratory.[23,24] Whereas the MQDT analysis of the *ungerade* np and nf states could be performed with high accuracy and played an important role in the most recent determination of the ionization and dissociation energies of H_2, HD, and D_2,[25–27] an MQDT analysis of the *gerade* nd Rydberg states with similar accuracy was not possible so far. The difficulties arising in the theoretical treatment of these states result from the fact that they are strongly perturbed by channel interactions with low-n, high-v^+ Rydberg states, which themselves are subject to perturbations by doubly-excited states. The situation is further complicated by the s-d interaction and by the hyperfine interaction in ortho-H_2, which completely mixes singlet and triplet character in the high-nd Rydberg states. The focus of the present work lies on the triplet *gerade* Rydberg states of H_2. Its goals were to obtain a complete map of the triplet nd Rydberg states with core vibrational quantum number $v^+ \leq 4$ in the range $n = 5$–30, to assign these states by combining double-resonance spectroscopic techniques and MQDT calculations, and to derive a reliable global

set of MQDT parameters for all triplet *gerade* states with $n = 2$–30 in a least-squares fit. Instead of printing long tables of the numerous states observed experimentally, we chose to list the complete set of experimental energy levels, including predictions of a large number of so far unobserved triplet ns and nd Rydberg states, in the Supporting Information.

A schematic energy-level diagram of the relevant states is presented in Figure 1. While states with $n \leq 4$ were extensively studied (see Refs. 1,2,28–38 and also Ref. 39 for a recompilation of some of the experimental data), we are not aware of any systematic analysis of triplet *gerade* Rydberg states with $n > 4$. Several groups studied high-nd triplet Rydberg states from the metastable $c\,^3\Pi_u^-$ state;[40–43] however, their spectra remained only partially analyzed, and neither vibrational perturbers nor ns Rydberg states could be definitely assigned. Dinu *et al.*[43] showed that, while the dominant decay channel for the triplet nd Rydberg states with $v^+ \leq 4$ lying below the adiabatic ionization threshold is predissociation, states above this threshold decay predominantly by autoionization. This behavior differs from that of states with $n \leq 4$ and $v^+ \geq 7$ which are subject to fast predissociation even above the ionization threshold, as was shown in a series of experiments by Helm and coworkers[44–47] and Siebbeles *et al.*[48] In particular the study of Lembo *et al.*[47] and a subsequent MQDT analysis by Matzkin *et al.*[49] demonstrated that, in the triplet manifold, perturbations by the *gerade* doubly-excited states become significant at internuclear distances larger than $4a_0$ (a_0 is the Bohr radius), and thus only directly affect Rydberg states with $v^+ \geq 6$. Rydberg states with $v^+ \leq 5$ might, however, be indirectly perturbed by doubly-excited states *via* vibrational channel interactions.

Experiment

A schematic diagram of the experimental configuration is displayed in Figure 2. H_2 in the metastable $c\,^3\Pi_u^-$ state (referred to as H_2^*) was produced by striking a discharge in a pulsed supersonic beam of pure H_2. The discharge took place between a tungsten filament and an electrode tip placed 15 mm and 20 mm downstream from the grounded nozzle plate, respectively. An ac current of 6.0 A and

50 Hz was run through the filament and a potential of $+700\,\mathrm{V}$ was applied to the electrode tip. A similar discharge setup was already used to produce metastable rare-gas atoms.[50,51] During the first few minutes of operation, the H_2^* density decreased by a factor of ~ 10, presumably because of the heating of the nozzle by the hot filament. The H_2^* density can be considerably increased by cooling the nozzle to around $-100\,^\circ\mathrm{C}$. The measurements presented in this work were, however, carried out without cooling. To prevent the H^+, H_2^+, and H_3^+ ions also produced in the discharge from entering the laser-excitation region, two deflection plates, one grounded and one held at $-250\,\mathrm{V}$, were placed between the electrode tip and the skimmer.

In the laser-excitation region, H_2^* was excited to autoionizing Rydberg states using the second harmonic of a commercial pulsed dye laser ($\lambda = 340 - 355\,\mathrm{nm}$, bandwidth $\sim 0.05\,\mathrm{cm}^{-1}$). 50 ns after the laser pulse, a pulsed voltage was applied across a set of resistively coupled extraction plates to accelerate the H_2^+ ions toward a microchannel-plate (MCP) detector. The laser-excitation region and the adjacent time-of-flight tube were surrounded by two concentric mumetal tubes to eliminate stray magnetic fields and reduce stray electric fields to below $5\,\mathrm{mV/cm}$. The spectra were obtained by monitoring the ratio between the H_2^+ ion signal and the laser intensity as a function of the wave number of the laser. The wave-number calibration was performed at an accuracy of $\sim 0.2\,\mathrm{cm}^{-1}$ by monitoring the radiation transmitted through an etalon of free spectral range $1.3\,\mathrm{cm}^{-1}$ and Ar-I transitions in an optogalvanic cell simultaneously with the H_2 spectrum.

Because the discharge produces many rovibrational levels of H_2^* and the Rydberg series accessible from these levels overlap spectrally, double-resonance experiments had to be performed to unambiguously determine the rovibrational quantum numbers of the initial levels. For this purpose, an additional, more intense pulsed UV laser (referred to as depletion laser) was overlapped spatially with the probe laser and used to deplete the population of selected $c^3\Pi_u^-$ levels 500 ns prior to the application of the probe laser. The wave number of the depletion laser was fixed at the positions of strong and well-known transitions so that the population of corresponding rovibrational levels of the metastable state was depleted by more than $50\,\%$. The electrons produced by the autoionizing Rydberg states excited by the depletion and probe lasers were extracted toward the

5

MCP detector by applying a small dc electric field of $-10\,\text{V/cm}$ and detected separately by setting temporal gates at the relevant positions of the time-of-flight spectrum. Such a small electric field has a negligible effect on the positions of the $n \leq 15$ Rydberg states assigned in this manner. The positive identification of the initial level of a transition induced by the probe laser was achieved by registering an increase (decrease) of the electron signal produced by the probe laser whenever the depletion laser was blocked (unblocked). Illustrative examples of this procedure are discussed below.

Observed spectrum

Vibrational and rotational structure

The spectrum of the autoionizing triplet Rydberg states of H_2 recorded from the metastable $c^3\Pi_\text{u}^-$ state is depicted in Figure 3. The spectral regions highlighted by the areas shaded in gray in Figure 3 are presented on enlarged scales in later figures. The rovibrational energy levels (v'', N'') of the metastable state in the range $v'' = 0$–4 and $N'' = 1$–5 are well known from measurements carried out by Dieke[2] and were corrected and extended in Ref. 39. The final Rydberg states converge to the $X^{+\,2}\Sigma_g^+$ electronic ground state of H_2^+ and are best described in Hund's angular-momentum coupling case (d). We use the notation $n\ell N_N^+(v^+)$, where n and ℓ are the principal and orbital-angular-momentum quantum numbers of the Rydberg electron, respectively, v^+ and N^+ are the vibrational and rotational quantum numbers of the H_2^+ ion core, respectively, and N is the total-angular-momentum quantum number ignoring spins. Spins could be ignored throughout this work because, in the final Rydberg states, the interactions involving spins (*i.e.* spin-spin, spin-orbit, spin-rotation, and hyperfine interactions) give rise to splittings that could not be observed at the experimental resolution of $0.05\,\text{cm}^{-1}$.

The term values $\tilde{\nu}$ of the Rydberg states relative to the $X^{1}\Sigma_g^+\,(v = 0, N = 0)$ ground state may be

converted into effective quantum defects δ using Rydberg's formula

$$\tilde{\nu} = \frac{E_i(H_2)}{hc} + \frac{E^+(v^+, N^+)}{hc} - \frac{R_{H_2}}{(n-\delta)^2},$$ (1)

where h is Planck's constant, c is the speed of light in vacuum, $E_i(H_2)/(hc) = 124417.4911(4)\,\text{cm}^{-1}$ is the adiabatic ionization energy of H_2,[25] $E^+(v^+, N^+)$ are the rovibrational energies of H_2^+ taken from *ab initio* calculations,[52,53] and $R_{H_2} = 109707.450\,\text{cm}^{-1}$ is the mass-corrected Rydberg constant for H_2. The effective quantum defect δ is approximately constant except when there are strong channel interactions, and therefore Eq. (1) is useful for an initial analysis of the spectra. Based on Rydberg's formula, the most prominent spectral patterns in Figure 3 can be identified as transitions from the $(v'' = 1–3, N'' = 1)$ states to Rydberg states with $v^+ = v''$, $N^+ = N'' = 1$ and δ close to 0 (see assignment bars in Figure 3). These transitions are assigned to nd Rydberg states because the transitions to the also allowed ns Rydberg states are about 30 times weaker.[40,41] Transitions with $\Delta v = v^+ - v'' = 0$ are strongly favored by the Franck-Condon principle, because the potential-energy curves of the metastable state of H_2 and the ground state of H_2^+ have a similar shape. Their intensity decreases and their positions shift to lower wave numbers with increasing v'' value. Transitions for which the change in the rotational quantum number $\Delta N = N^+ - N''$ is zero are also strongly favored.

Shifts toward lower wave numbers of the transitions occurring at increasing $v^+ = v''$ values originate from the reduced vibrational spacing of H_2^+ compared to the vibrational spacing of the metastable state. There are two reasons why the intensity of the transitions decreases with increasing vibrational excitation: Firstly, the higher vibrational levels of the metastable state are less populated in the discharge because the Franck-Condon factor for the excitation from the vibronic ground state of H_2 decreases.[42] Secondly, the lifetime of the metastable state decreases with vibrational excitation,[54] leading to a partial decay of the population of metastable H_2 in higher vibrational states during the $\sim 100\,\mu s$ flight time from the discharge region to the laser-excitation region (see Figure 2). Overall, the linewidths of the transitions on the low-n side of the spec-

trum are larger than those on the high-n side. This effect primarily originates from the slower autoionization dynamics of high-n Rydberg states. However, we cannot exclude that saturation also contributes to the observed broadening at low n values. Although autoionization resonances can in principle have asymmetric Fano line shapes, in the present case, the almost perfectly diagonal nature of the Franck-Condon factors leads to symmetric Lorentz line shapes, *i.e.* Fano profiles with large q factors.

The spectrum near the $27\mathrm{d}1_N(1) \leftarrow (1,1)$ transitions is displayed on a enlarged scale in Figure 4. The splittings in this part of the spectrum are caused by the rotational structure and the orbital fine structure resulting from the coupling between $\vec{N}^+$ and $\vec{\ell}$,

$$\vec{N} = \vec{N}^+ + \vec{\ell}. \tag{2}$$

The $\Delta N = N^+ - N'' = 0$ transitions with increasing $N^+ = N''$ values are shifted toward lower wave numbers because the rotational spacings of H_2^+ are slightly smaller than the rotational spacings of the metastable state. The reduced intensity of the transitions from $N'' = 2$ compared to those from $N'' = 1$ reflects the lower spin-statistical weight of para-H_2 ($g_{ss} = 1$) compared to ortho-H_2 ($g_{ss} = 3$). No transitions to $N^+ = 0$ Rydberg states are observed in this part of the spectrum because the $c^3\Pi_u^-$ state does not possess a $N'' = 0$ state. From the reduced intensity of the transitions from $N'' = 3$ compared to those from $N'' = 1$, one can estimate the rotational temperature of the metastable H_2 molecules to be about $230\,\mathrm{K}$. The discharge thus appears to increase the rotational temperature of the H_2 sample. Despite this heating effect, no transitions from states with $N'' > 3$ were observed.

Selection rules and orbital fine structure

The Rydberg electron in the $c^3\Pi_u^-$ state has predominant p character so that the $\Delta\ell = \pm 1$ selection rule permits only transitions to ns and nd Rydberg states to occur strongly, whereas transitions to g states ($\ell = 4$) and higher partial waves are expected to be very weak and are not further considered here. The parity selection rule for electric-dipole transitions limits the change in the

rotational quantum number $\Delta N = N^+ - N''$ to even values because the total parities of the Π^- initial and *gerade* final states are given by $-(-1)^{N''}$ and $(-1)^{N^+}$, respectively. The total-angular-momentum conservation rule further restricts transitions to Rydberg states with $N = N''$ or $N = N'' \pm 1$. Combining these selection rules and considering the relation given in Eq. (2) leads to the following set of allowed transitions:

$$ n\text{s1}_1, \underline{n\text{d1}_{1,2}}, n\text{d3}_{1,2} \quad \leftarrow \quad (v'', N'' = 1), \tag{3} $$

$$ n\text{s2}_2, n\text{d0}_2, \underline{n\text{d2}_{1,2,3}}, n\text{d4}_{2,3} \quad \leftarrow \quad (v'', N'' = 2), \tag{4} $$

$$ n\text{s3}_3, n\text{d1}_{2,3}, \underline{n\text{d3}_{2,3,4}}, n\text{d5}_{3,4} \quad \leftarrow \quad (v'', N'' = 3). \tag{5} $$

The most intense Rydberg series observed in Figure 3, *i.e.* the nd Rydberg series with $\Delta N = 0$, are underlined in Eqs. (3)–(5). No strict selection rule exists for the vibrational quantum number; however, $\Delta v = v^+ - v'' = 0$ transitions have by far the largest Franck-Condon factors as explained above.

The observed Rydberg states are subject to weak orbital fine splittings corresponding to the angular-momentum coupling described by Eq. (2). In nd Rydberg states, the orbital fine structure consists of three components for $N^+ = 1$ and five components for larger values of N^+. In Figure 4, only two components are observed for $N^+ = 1$, and three components for $N^+ = 2$ and 3, because the electric-dipole selection rules given in Eqs. (3)–(5) exclude the other components. The magnitude of the orbital fine structure scales as n^{-3} and decreases with increasing N^+ value. The latter effect results from the increasing coupling of $\vec{\ell}$ to the axis of rotation as N^+ increases.[55] In the limit of pure Hund's case (d), the orbital fine components become degenerate. The orbital fine splitting can be calculated using MQDT as will be discussed below. In Figs. 3 and 4, the orbital fine component with $N = N^+ + 1$ is usually the most intense, and the $N = N^+ - 1$ component (for $N^+ \geq 2$) the weakest.

The metastable state and determination of term values

The splittings resulting from the spin fine structure of the metastable state is partially resolved for the narrow transitions on the high-n side of the spectrum, as illustrated for two transitions from $(v'', N'') = (1, 1)$ and $(1, 2)$ in Figs. 5a and 5b, respectively. The expected spin fine splittings of the metastable state are well known[56] and are indicated as vertical dashed lines. The three components are labeled F_1, F_2, and F_3 for $J'' = N'' - 1, J'' = N''$, and $J'' = N'' + 1$, respectively. The F_1 and F_3 components are separated by less than $0.05\,\text{cm}^{-1}$ and could not be resolved in the present experiment. In contrast, the F_2 component is separated from the F_1 component by $\sim 0.2\,\text{cm}^{-1}$ and is clearly visible on the low-wave-number side of the transitions. The intensity of transitions from the F_2 component compared to F_1 and F_3 components is, however, considerably smaller than expected from the degeneracy factors alone. This observation has its origin in the shorter lifetimes of the F_2 components compared to the F_1 and F_3 components.[54]

The transition wave numbers were determined by fitting a Gaussian line shape to the observed peaks assigned to the unresolved F_1 and F_3 components and correcting for the deviation between the F_1 and F_3 components and the center of gravity of all three components. For transitions with $v'' > 1$, the spin fine structure was obtained by linearly extrapolating the coupling constants of the $v'' = 0$ and 1 levels reported in Ref. 56. Due to the reduced intensity of the F_2 component, the correction was also added for transitions for which the spin fine splitting could not be resolved. Note that the correction does not exceed the experimental uncertainty of $\pm 0.2\,\text{cm}^{-1}$ and ranges from $-0.07\,\text{cm}^{-1}$ for the $(1, 1)$ state to $-0.05\,\text{cm}^{-1}$ for the $(4, 3)$ state.

The term values of the observed Rydberg states relative to the $X\,^1\Sigma_g^+$ $(v = 0, N = 0)$ ground state of H_2 were obtained by adding the observed transitions wave numbers to the known positions of the metastable state.[39] In the course of the analysis, we found that the term values of the $c\,^3\Pi_u^-$ $(v'' = 1-4, N'' = 1-3)$ levels given in Ref. 39 are consistent with our results within $0.2\,\text{cm}^{-1}$, except the $(4, 2)$ and $(4, 3)$ levels which were reported to be located $103677.21\,\text{cm}^{-1}$ and $103822.83\,\text{cm}^{-1}$ above the ground state, respectively, whereas we find their positions to be $103676.06\,\text{cm}^{-1}$ and $103823.18\,\text{cm}^{-1}$, respectively. The term values of the $n\text{d}1_{1,2}(1)$ Rydberg series observed from the

$(1, 1)$ state are listed in Table 1 and a complete list of all observed Rydberg states is provided as Supporting Information. The observed term values are transformed using Eq. (1) into effective quantum defects δ which are also given in Table 1. For an unperturbed Rydberg series one would expect δ to be constant. The observed fluctuations of δ are characteristic of rovibrational channel interactions.

Rotational and vibrational channel interactions

Rydberg series can be perturbed by Rydberg states of lower n values but higher rotational and/or vibrational quantum numbers which lie in the same energy region. Several potential vibrational perturbers can be identified in Figure 1. The $n = 6, v^+ = 4$ Rydberg states, for instance, is expected to perturb the $v^+ = 3$ Rydberg series between $n = 9$ and $n = 10$. Perturbers must have the same parity and the same N value as the Rydberg series they interact with. Channel interactions represent prototypical examples of nonadiabatic coupling of the electronic and nuclear motions, modify both the intensity distribution and the spectral positions of the otherwise regular Rydberg series, and are omnipresent in the spectra of Rydberg states of H_2. In some cases, the interactions are so large that it is not possible to distinguish between perturbing and perturbed Rydberg states.

The narrow wave-number range between $28255 \, \text{cm}^{-1}$ and $28325 \, \text{cm}^{-1}$ displayed on an enlarged scale in Figure 6 is well suited to demonstrate the omnipresence of channel interactions in the triplet *gerade* spectrum of H_2. In this region one indeed observes $|\Delta v^+| = 1$ vibrational channel interactions, *e.g.* between the $10\text{d}1_1 \, (v^+ = 1)$ and the $6\text{d}1_1 \, (v^+ = 2)$ states (lines **F** and **F'** in Figure 6), which are the strongest vibrational channel interactions, and $|\Delta N^+| = 2$ rotational channel interactions, *e.g.* between the $10\text{d}1_2 \, (v^+ = 1)$ and the $9\text{d}3_2 \, (v^+ = 1)$ states (lines **C** and **C'**), which are the strongest rotational channel interactions. The lines **C** and **C'** may be assigned to the $10\text{d}1_2 \, (1) \leftarrow (1, 1)$ and the $9\text{d}3_2 \, (1) \leftarrow (1, 1)$ transitions. Although the $\Delta N = N^+ - N'' = 2$ transition to the $9\text{d}3_2 \, (1)$ state is expected to be weak and the $\Delta N = 0$ transition to the $10\text{d}1_2 \, (1)$ state to be strong, their intensities are approximately equal and about half of the intensity of the transition to the next member of the $n\text{d}1_2 \, (1)$ series near $28475 \, \text{cm}^{-1}$ (see Figure 3). We assigned the lower of these two lines

11

(**C'**) to the $10d1_2(1) \leftarrow (1,1)$ transition, and the higher one (**C**) to the $9d3_2(1) \leftarrow (1,1)$ transition. The rotational channel interaction shifts the $10d1_2(1)$ state to lower wave numbers which leads to the large value of the effective quantum defect δ in Table 1 when compared to other members of the Rydberg series. The transition to the $9d3_2(1)$ state is correspondingly shifted to higher wave numbers and gains intensity through the almost complete mixing with the $10d1_2(1)$ state.

A detailed analysis of the spectrum displayed in Figure 6 leads to the identification of no less than eight rovibrational perturbers labeled **A–H**. The resulting level shifts and modification of the intensity distributions render the spectrum extremely difficult to assign. Indeed, assignments of the perturbers based on Rydberg's formula cannot be made with absolute certainty: Even if the quantum defect of a vibrational perturber with $n = 6$ were known with an uncertainty of only 0.02, the uncertainty in the spectral position would still be as high as $20\,\text{cm}^{-1}$. A complete assignment and quantitative analysis of the spectrum necessitate therefore a rigorous treatment of all possible interactions with all possible ionization channels. Multichannel quantum-defect theory offers the ideal framework for such a treatment.

Quantitative analysis

Multichannel quantum-defect theory

To complete the assignment of the observed spectrum and to quantitatively analyze the structure of the observed Rydberg states, we used multichannel quantum-defect theory (MQDT) adapted to the calculation of bound states in molecules as described in Refs. 9,18,57,58. Several versions of MQDT exist which differ in the normalization of the Coulomb function pair employed to expand the wave function of the Rydberg electron, and also in the form of the irregular component added to account for core effects.[39,59] In this work, we used the η-formalism,[17–19] which leads, for a given total parity $(-1)^p$ and a given total-angular-momentum quantum number N, to the following

condition for the existence of a bound state with energy E:

$$\det \left| \tan\left[\pi \mathbf{v}(E)\right] \mathbf{A}^{-1}(E) + \mathbf{K}^{(Np)}(E) \right| = 0. \tag{6}$$

In Eq. (6), $\mathbf{K}^{(Np)}$ is the full rovibronic reaction matrix discussed below, and $\mathbf{v}$ and $\mathbf{A}$ are matrices containing the effective principal quantum numbers and Ham's scaling factors, respectively. These three matrices have to be determined in Hund's case (d) for which $i = (\ell, v^+, N^+)$ are good quantum numbers. Quantum numbers associated with the electronic motion of the ion core are not used because we only consider the $X^+\,{}^2\Sigma_g^+$ ground state of H_2^+ in our analysis. In Hund's case (d), $\mathbf{v}$ and $\mathbf{A}$ are both diagonal and their elements are given by

$$v_{ii}(E) = \sqrt{\frac{hcR_{H_2}}{E_i(H_2) + E^+(v^+, N^+) - E}} \tag{7}$$

and

$$A_{ii}(E) = \prod_{j=0}^{\ell}\left(1 - \frac{j^2}{v_{ii}(E)^2}\right). \tag{8}$$

All quantities used in Eq. (7) have already been introduced in the previous section. Open channels, *i.e.* channels for which the denominator in Eq. (7) is negative, are removed from the calculation, which implies that shifts caused by interactions with the ionization continua are neglected. In general, this is a good approximation because such shifts are expected to be smaller than the observed autoionization linewidths.

For the construction of the reaction matrix $\mathbf{K}^{(Np)}(E)$ from the eigenquantum defects $\eta_{\ell\ell'}^{(\Lambda)}(R, E)$, we follow the procedure described in Sec. III B of Ref. 18 and evaluate

$$\mathbf{K}^{(Np)}(E) = \mathbf{V}\tan\left(\pi\mathbf{V}^\dagger\boldsymbol{\eta}^{(Np)}(E)\mathbf{V}\right)\mathbf{V}^\dagger \tag{9}$$

with

$$\eta_{ii'}^{(Np)}(E) = \sum_{\Lambda} U_{N^+\Lambda}^{(Np\ell)}\left[\int_0^{\infty} \chi_{v^+}^{(N^+)}(R)\eta_{\ell\ell'}^{(\Lambda)}(R,E)\chi_{v^{+\prime}}^{(N^{+\prime})}(R)\,\mathrm{d}R\right]U_{\Lambda N^{+\prime}}^{(Np\ell')}. \tag{10}$$

13

In Eqs. (9) and (10), $\boldsymbol{\eta}^{(Np)}$ is the quantum-defect matrix in Hund's case (d), $\boldsymbol{V}$ is the eigenvector matrix of $\boldsymbol{\eta}^{(Np)}$ [$\boldsymbol{V}^\dagger \boldsymbol{\eta}^{(Np)}(E)\boldsymbol{V}$ is diagonal], Λ is the quantum number associated with the projection of $\vec{N}$ onto the internuclear axis, $\boldsymbol{U}$ is the rotational frame-transformation matrix discussed below, R is the internuclear distance, and χ are the vibrational wave functions of the electronic ground state of the H_2^+ ion core. Note that the eigenquantum-defect parameters $\eta_{\ell\ell'}^{(\Lambda)}(R,E)$ used here do not correspond exactly to the η eigenquantum defects used in Ref. 18 but to their functions $M^\Lambda(R)$. The advantages of using Eqs. (9) and (10) to construct the rovibronic reaction matrix were first recognized and discussed by Du and Greene.[60]

The rotational frame-transformation matrix $\boldsymbol{U}$ is given by the unitary transformation from Hund's case (b) to Hund's case (d). The elements of $\boldsymbol{U}$ are given by (see, *e.g.*, Eq. (B2) of Ref. 61):

$$U_{N^+\Lambda}^{(Np\ell)} = (-1)^{N-\Lambda} \frac{1+(-1)^{p-N^++\ell}}{2} \sqrt{\frac{4N^++2}{1+\delta_{\Lambda0}}} \begin{pmatrix} N^+ & \ell & N \\ 0 & \Lambda & -\Lambda \end{pmatrix}, \tag{11}$$

where δ is the Kronecker delta and the last factor represents a Wigner 3-j symbol. In the following we use the electronic parity (positive for Λ^+ states and negative for Λ^- states) instead of the total parity $(-1)^p$. The electronic parity is equal (opposite) to the total parity for even (odd) values of N. For a given electronic parity and N value, the contributing s and d channels of both limiting coupling cases are listed in Table 2. In Hund's case (d), *gerade* Rydberg states have positive (negative) electronic parity if $N-N^+$ is even (odd).

Determination of the *ab initio* eigenquantum-defect curves

MQDT describes the triplet ns and nd Rydberg states in terms of five eigenquantum-defect functions $\eta_{ss}^{(\Sigma)}(R,E), \eta_{sd}^{(\Sigma)}(R,E), \eta_{dd}^{(\Sigma)}(R,E), \eta_{dd}^{(\Pi)}(R,E)$, and $\eta_{dd}^{(\Delta)}(R,E)$, which we derive using the method described in Ref. 17. We use Born-Oppenheimer (BO) potential-energy curves of the lowest five $^3\Sigma_g^+$ states,[62,63] three $^3\Pi_g$ states,[62,64] and two $^3\Delta_g$ states[65] available in the literature. The BO

energy $E(R)$ is first transformed to the energy of the Rydberg electron (in Rydberg units)

$$\varepsilon(R) = \frac{E(R) - E^+(R)}{hcR_\infty}. \tag{12}$$

In Eq. (12), $R_\infty = 109737.316\,\text{cm}^{-1}$ is the Rydberg constant and $E^+(R)$ is the BO energy of the $X^{+\,2}\Sigma_g^+$ ground state of H_2^+ taken from Ref. 66. Each point $\varepsilon(R)$ of a BO potential-energy curve has to fulfill the equation

$$\det\left|\tan\left[\pi\nu(\varepsilon)\right]A^{-1}(\varepsilon) + K^{(\Lambda)}(\varepsilon)\right| = 0. \tag{13}$$

Eq. (13) is the Hund's-case-(b) analogue of Eq. (6). The matrices ν and A are again diagonal and their elements are given by

$$\nu_{\ell\ell}(\varepsilon) = \sqrt{\frac{1}{-\varepsilon}} \tag{14}$$

and

$$A_{\ell\ell}(\varepsilon) = \prod_{j=0}^{\ell}\left(1 - \frac{j^2}{\nu_{\ell\ell}(\varepsilon)^2}\right). \tag{15}$$

The reaction matrix $K^{(\Lambda)}$ in Hund's case (b) is obtained in analogy to Eq. (9) using

$$K^{(\Lambda)}(\varepsilon) = V\tan\left(\pi V^\dagger \eta^{(\Lambda)}(\varepsilon)V\right)V^\dagger, \tag{16}$$

where V is the eigenvector matrix of $\eta^{(\Lambda)}(\varepsilon)$ [$V^\dagger\eta^{(\Lambda)}(\varepsilon)V$ is diagonal].

The matrices in Eq. (13) are two-dimensional for the $^3\Sigma_g^+$ symmetry and one-dimensional for larger values of Λ because the s channel does not exist in the latter case. For the $^3\Pi_g$ symmetry, highly-accurate *ab initio* calculations are available for the $3\mathrm{d}\pi i$ state,[62] the $4\mathrm{d}\pi r$ state,[62] and the $5\mathrm{d}\pi w$ state.[64] Solving Eq. (13) using these three potential-energy curves leads to three values for $\eta_{\mathrm{dd}}^{(\Pi)}(R,\varepsilon)$ at each internuclear distance R. Because the states have $n = 3$, $n = 4$, and $n = 5$, the three values of $\eta_{\mathrm{dd}}^{(\Pi)}(R,\varepsilon)$ are obtained near $\varepsilon = -1/3^2$, $\varepsilon = -1/4^2$, and $\varepsilon = -1/5^2$, respectively. The eigenquantum defects at arbitrary values of ε are obtained by extrapolation using a quadratic polynomial in ε. The resulting *ab initio* eigenquantum-defect curves $\eta_{\mathrm{dd}}^{(\Pi)}(R,\varepsilon)$ for $\varepsilon = -1/3^2$, $\varepsilon =$

$-1/4^2$, and $\varepsilon = 0$ are depicted in Figure 7d as dotted, dashed, and solid lines, respectively.

For the $^3\Delta_g$ symmetry, highly-accurate *ab initio* calculations are only available for two states, namely the 3d$\delta\,j$ and the 4d$\delta\,s$ states.[65] The same procedure as for the $^3\Pi_g$ states can be applied, except that the extrapolation to arbitrary values of ε is performed using a linear polynomial in ε. The resulting eigenquantum defects $\eta_{dd}^{(\Delta)}$ are depicted in Figure 7e.

The situation is more complex for the $^3\Sigma_g^+$ symmetry because, in this case, Eq. (13) has two diagonal contributions (ss and dd) and one off-diagonal contribution for each value of R. It is therefore not possible to directly extract eigenquantum-defect parameters from the potential-energy curves. Instead, we follow Ref. 17 and assume that the shape of the s-d interaction in the relevant range of internuclear distances is given by

$$\eta_{sd}^{(\Sigma)}(R, \varepsilon = -1/3^2) = \alpha_3 R^2 \tag{17}$$

and

$$\eta_{sd}^{(\Sigma)}(R, \varepsilon = -1/4^2) = \alpha_4 R^2. \tag{18}$$

The s-d interaction at arbitrary values of ε is obtained by linear extrapolation. The choice of quadratic functions in Eqs. (17) and (18) is somewhat arbitrary, but is motivated by the fact that the s-d interaction vanishes at $R = 0$. We first choose values $\alpha_3 = \alpha_4 = -0.0035\,a_0^{-2}$ and set up, for a fixed value of R, a system of five equations by inserting the potential energy of the 2s$\sigma\,a$ state,[62] the 3s$\sigma\,h$ state,[62] the 3d$\sigma\,g$ state,[62] the 4sσ state,[63] and the 4dσ state[63] into Eq. (13) *via* Eq. (12). This system of equations is solved numerically for five parameters which we choose to be the ss eigenquantum defects at $\varepsilon = -1/2^2, -1/3^2, -1/4^2$, and the dd eigenquantum defects at $\varepsilon = -1/3^2, -1/4^2$. From these parameters, the ss and dd eigenquantum defects at arbitrary values of ε are obtained by quadratic and linear extrapolation, respectively. Solving the system of equations for a grid of internuclear distances between $R = 1.0\,a_0$ and $R = 5.0\,a_0$ leads to eigenquantum-defect curves which, for $\varepsilon = -1/3^2$ and $\varepsilon = -1/4^2$, are not smooth in the region between $R = 1.7\,a_0$ and $R = 2.2\,a_0$ because of avoided crossings between the corresponding potential-energy curves. This indicates

that the s-d interaction is not optimal for the initially chosen values of α_3 and α_4. We therefore adjust α_3 and α_4 until the ss and dd eigenquantum-defect curves at $\varepsilon = -1/3^2$ and $\varepsilon = -1/4^2$ are as smooth as possible. The optimal values of α_3 and α_4 are -0.00280 and -0.00268, respectively and correspond to the eigenquantum defects $\eta_{\text{ss}}^{(\Sigma)}, \eta_{\text{sd}}^{(\Sigma)}$, and $\eta_{\text{dd}}^{(\Sigma)}$ depicted in Figs. 7a–c.

Mass dependence of the clamped-nuclei eigenquantum defects

Once the clamped-nuclei eigenquantum defects $\eta_{\ell\ell'}^{(\Lambda)}(R,\varepsilon)$ were determined, correction terms accounting for the finite mass of the nuclei were added. Although the use of the mass-corrected Rydberg constant in Eq. (7) already includes part of the finite-mass correction, two additional small Rydberg-electron–core interaction terms must be added separately as discussed in detail in Ref. 18. These contributions depend on the nuclear masses and correspond to the 'normal' and the 'specific' mass effect (mass-polarization term). Both terms may contribute up to a few cm^{-1} to the energy of the lowest Rydberg states, and thus have to be considered if, as is our aim here, the Rydberg structure from $n = 2$ or 3 up to $n \approx 45$ is to be represented in a single MQDT calculation to within a fraction of a wavenumber unit. The 'normal' mass correction only contributes to the diagonal eigenquantum-defect matrix elements and is given by [18]

$$\Delta_{\text{nm}}\eta_{\ell\ell}^{(\Lambda)}(R) = -\frac{1}{4(\mu/m)}R\frac{\partial\eta_{\ell\ell}^{(\Lambda)}}{\partial R}, \tag{19}$$

where $\mu/m = 918.076$ is the nuclear reduced mass of H$_2$ in atomic units. For all calculations presented in this work, the 'normal' mass correction was evaluated numerically at $\varepsilon = 0$ and added to the clamped-nuclei eigenquantum defects $\eta_{\ell\ell}^{(\Lambda)}(R,\varepsilon)$ before they were used in Eq. (10).

The 'specific' mass effect represents a second correction [9]

$$\Delta_{\text{sm}}\eta_{\ell\ell}^{(\Lambda)}(R) = -\frac{1}{4(\mu/m)}n^{*3}\langle n^*\ell\Lambda(R)|a_0^2\nabla_1\nabla_2|n^*\ell\Lambda(R)\rangle . \tag{20}$$

In Eq. (20), the gradient operators ∇_1 and ∇_2 act on the Rydberg and the core electron, respectively,

and $n^* = n - \delta$ is the effective principal quantum number. The evaluation of this term requires accurate first-principles electronic wavefunctions for a given Rydberg state $|n^*\ell\Lambda\rangle(R)$; in the quantum-chemical papers usually the quantity $H'_3(R) = 2R_\infty(m/4\mu)\langle n^*\ell\Lambda(R)|a_0^2\nabla_1\nabla_2|n^*\ell\Lambda(R)\rangle$, in cm^{-1}, is given. For the $2s\sigma a$ state of H_2, $H'_3(R)$ has been calculated by Kolos and Rychlewski and amounts to $0.6\,\mathrm{cm}^{-1}$ around $R = 2a_0$.[67] From these *ab initio* calculations the 'specific' mass contribution to $\eta_{ss}^{(\Sigma)}$ was evaluated using Eq. (20) and is given in the last column of Table 6. For the 3d states, the 'specific' mass corrections are smaller and H'_3 is on the order of $0.1\,\mathrm{cm}^{-1}$,[68] *i.e.* less than the level of accuracy considered in this work.

We have not taken account of the 'specific' mass effect in our *ab initio* MQDT calculations designed to assign the spectra for $n > 4$ where it is not important, but we included its contribution to the ssΣ channel in the subsequent adjustments of the eigenquantum defects to experimental data in the range $n = 2$–30 which are discussed below.

Numerical implementation of MQDT

The *ab initio* rovibronic energies of the triplet ns and nd Rydberg states of H_2 were found by numerically solving Eq. (6) using the eigenquantum defects determined as described in the previous section. Whereas the matrices $\boldsymbol{\nu}$ and $\boldsymbol{A}$ follow immediately from Eqs. (7) and (8), there is no unique way to evaluate $\boldsymbol{K}^{(Np)}$ using Eqs. (9) and (10). The ambiguity arises from the fact that in the current treatment the eigenquantum defects do not depend on the total energy E but only on the energy of the Rydberg electron ε. There are many possibilities to divide the total energy into the energy of the Rydberg electron and the energy of the ion core.[69] In Hund's case (b), *e.g.*, the relation between E and ε is given by Eq. (12). Here we follow the approach explained in chapter 4.2.5 of Ref. 58 and use in Eq. (10) the eigenquantum defects at

$$\varepsilon = \frac{E - E_0}{hcR_\infty} \tag{21}$$

with

$$E_0 = E_i + \frac{1}{2}\left[E^+(v^+, N^+) + E^+(v^{+\prime}, N^{+\prime})\right].\tag{22}$$

Because the evaluation of Eq. (10) at each trial energy E is computationally expensive, we expand the eigenquantum-defect curves in a Taylor series in ε around $\varepsilon = 0$:

$$\eta_{\ell\ell'}^{(\Lambda)}(R, \varepsilon) = \sum_{k=0}^{k_{max}} \frac{\varepsilon^k}{k!} \frac{\partial^k \eta_{\ell\ell'}^{(\Lambda)}(R, \varepsilon = 0)}{\partial \varepsilon^k}.\tag{23}$$

Note that with our choice of $k_{max} = 2$, Eq. (23) perfectly describes the *ab initio* eigenquantum defects because these were constructed either as linear or quadratic polynomials in ε (see above). In the same way as $\eta_{\ell\ell'}^{(\Lambda)}$ is transformed to Hund's-case-(d) eigenquantum defects $\eta_{ii'}^{(Np)}$ in Eq. (10), the energy-independent Taylor coefficients $\frac{\partial^k \eta_{\ell\ell'}^{(\Lambda)}}{\partial \varepsilon^k}$ are transformed to $\frac{\partial^k \eta_{ii'}^{(Np)}}{\partial \varepsilon^k}$. Consequently, the Hund's-case-(d) eigenquantum defects are expressed as[58]

$$\eta_{ii'}^{(Np)}(E) = \sum_{k=0}^{2} \frac{1}{k!} \frac{\partial^k \eta_{ii'}^{(Np)}}{\partial \varepsilon^k} \left(\frac{E - E_0}{hcR_\infty}\right)^k.\tag{24}$$

The advantage of using Eq. (24) is that Eq. (10) does not have to be evaluated at each energy E, but only once for each Taylor coefficient.

The vibrational wave functions of H_2^+ used in Eq. (10) were calculated from the potential-energy curve including adiabatic corrections from Ref. 66 using the Numerov-Cooley algorithm on a grid with spacing $0.005\,a_0$ ranging from $R_{min} = 1.0\,a_0$ to $R_{max} = 12\,a_0$. The integral in Eq. (10) was evaluated on the same grid using the eigenquantum defects determined for $R \le 5\,a_0$. The rovibrational energies of H_2^+ used in Eq. (7) were taken from nonadiabatic *ab initio* calculations[52,53] for $v^+ \le 10$ and from our adiabatic calculations mentioned above for larger values of v^+. The calculated Rydberg level energies did not depend on the values of the eigenquantum defect functions beyond $R = 5\,a_0$, as was tested for all levels calculated in this work. A second test which was carried out for all calculated energies is the convergence with respect to an increase of the maximal vibrational quantum number v_{max}^+ included in the basis set. All calculations published in this work

were converged to within $0.1\,\mathrm{cm}^{-1}$ when using $v^+_{\mathrm{max}} = 10$ except those for the $2\mathrm{s}\sigma\,a$ state, for which the basis had to be extended to $v^+_{\mathrm{max}} = 15$. These tests indicate that the present implementation of the approach is meaningful.

Assignment of transitions to rotational and vibrational perturbers

The assignment of Rydberg series at n values beyond 15 is usually straightforward and can be carried out using Rydberg's formula. In contrast, the assignments of low-n states is very challenging and necessitates the combined use of double-resonance measurements and *ab initio* MQDT calculations. The results of the *ab initio* MQDT calculations for all triplet *gerade* states of H_2 with $n \leq 4$ are compared to experimental data from the literature in Table 3.[2,30,32,38,39] For clarity, we only present the results for states with $N = 2$ in Table 3, but the agreement between experimental and calculated levels is similar for the other N values, as can be seen in the Supporting Information. The agreement is on the order of $1\,\mathrm{cm}^{-1}$ as was the case in similar studies.[19,39] For the states with $n = 3$, vibrationally excited states with $v \geq 3$ had to be omitted from our calculations because the results did not converge even when using a basis with $v^+_{\mathrm{max}} = 40$. A calculation of these states would be possible by explicitly taking into account electronically excited states of H_2^+ and evaluating the eigenquantum defects beyond $R = 5\,a_0$,[19,39] but was not carried out in the realm of the present investigation. For the $n \geq 4$ Rydberg states, the calculation of all states with $v^+ \leq 4$ could be performed.

An error $\Delta\eta$ in the eigenquantum defects leads to a deviation

$$\Delta\tilde{\nu} \approx -\frac{2R_{H_2}}{(n-\delta)^3}\Delta\eta \tag{25}$$

between the calculated and exact term value. The mean deviations between the observed and *ab initio* term values for the $n = 2, 3$, and 4 states amount to $\Delta\tilde{\nu} = 0.1\,\mathrm{cm}^{-1}, 0.4\,\mathrm{cm}^{-1}$, and $0.1\,\mathrm{cm}^{-1}$, respectively. Using Eq. (25), we can therefore estimate that $\Delta\eta$ is 4×10^{-6}, 5×10^{-5}, and 3×10^{-5} for the $n = 2$, $n = 3$, and $n = 4$ states, respectively. The value of $\Delta\eta$ at higher n values is expected

to increase because the energy dependence of the eigenquantum defects is not known *a priori* and had to be extrapolated from the low-*n* states.

In the previous section we assigned Rydberg states with $n \geq 10$ on the basis of Rydberg's formula (see Table 1 for the $n\mathrm{d}1_N(1)$ series). The *ab initio* MQDT calculations for these states are also included in this table for comparison. The agreement between the observed and calculated term values is better than $1\,\mathrm{cm}^{-1}$, except for the $10\mathrm{d}1_1(1)$ state which is subject to strong rovibrational channel interactions, as already discussed above. For states with n higher than ~ 18, the deviations between observed and calculated positions correspond to the experimental uncertainty of $0.2\,\mathrm{cm}^{-1}$. We can therefore estimate the uncertainties in the eigenquantum defects to be $\Delta\eta = 0.005$ at energies corresponding to the high-*n* Rydberg states ($\varepsilon \approx 0$). This value of $\Delta\eta$ corresponds to uncertainties in the term values calculated *ab initio* of $\Delta\tilde{\nu} = 1\,\mathrm{cm}^{-1}$ at $n = 10$ and $\Delta\tilde{\nu} = 5\,\mathrm{cm}^{-1}$ at $n = 6$. This accuracy was sufficient to make preliminary assignments of all transitions observed in the realm of this work.

To experimentally confirm or correct the tentative assignments based on MQDT calculations, the double-resonance technique described in the experimental section was employed. Figure 8 shows the temporal evolution of the electron signal from the probe laser as the depletion laser is blocked and unblocked for three representative cases (a)–(c). For all three traces the depletion laser was fixed at a wave number of $28296\,\mathrm{cm}^{-1}$, so as to deplete the $c^3\Pi_\mathrm{u}^-$ ($v'' = 1, N'' = 1$) level using the $9\mathrm{d}3_2(1) \leftarrow (1,1)$ transition (see line **C** in Figure 6 above). The electron signal originating from the probe laser when it is tuned to line **B** in Figure 6 is shown in panel (a) of Figure 8. Initially both lasers are on and after about 10 s the depletion laser is blocked. The increase in signal from 0.15 to 1 proves that transition **B** also originates from the $(1, 1)$ state and that the depletion laser removed about 85 % of the initial population in the $(1, 1)$ state. With the initial state experimentally assigned, the term value of the final state of transition **B** can be determined. An important advantage of this double-resonance technique is that it makes assignments also possible for very weak transitions. An example is depicted in Panel (b) of Figure 8 where the probe laser is tuned to line **J** displayed in Figure 9. Although the signal-to-noise ratio of this measurement is poorer, a pronounced increase

in electron signal is observed when the depletion laser is blocked. When the transition driven by the probe laser does not originate from the same level as the transition induced by the depletion laser, no increase in electron signal is detected upon blocking this laser (see Figure 8c). The same procedure was used for all initial levels of the $c\,^3\Pi_u^-$ state with $v'' = 1\text{–}4$ and $N'' = 1\text{–}3$, whenever the assignment of the transitions on the basis of Rydberg's formula was not straightforward. A total of 57 transitions to ns and nd Rydberg states were assigned in this manner.

The assignments of the 16 lines labeled **A–P** in Figs. 6 and 9 to transitions to rovibrational perturbers are given in Table 4. The deviations between observed term values and term values calculated *ab initio* are less than $5\,\mathrm{cm}^{-1}$, as expected from the above considerations. Over the whole spectrum, a total of 372 transitions to 366 different final Rydberg levels could be assigned, 5 corresponding to ns states and 361 to nd states ($4 \leq n \leq 45$). Their term values as well as the comparison to values determined by MQDT are provided as Supporting Information.

Adjustment of the eigenquantum-defect curves

To further improve the triplet *gerade* eigenquantum defects of molecular hydrogen, especially at high energies, we adjusted their values until perfect agreement between calculated and observed energy levels was achieved. To avoid the simultaneous optimization of a large number of fit parameters, the fitting procedure was divided into two steps. In the first step, we only considered the levels with negative electronic parity, the positions of which do not depend on any eigenquantum-defect parameter of Σ symmetry (see Table 2), and adjusted the $\mathrm{dd}\,\Pi$ and $\mathrm{dd}\,\Delta$ eigenquantum defects. In the second step, we only considered the levels with positive electronic parity. The $\mathrm{dd}\,\Pi$ and $\mathrm{dd}\,\Delta$ eigenquantum defects were held fixed and only the $\mathrm{ss}\,\Sigma, \mathrm{sd}\,\Sigma$, and $\mathrm{dd}\,\Sigma$ eigenquantum defects were adjusted.

The adjustment of the *ab initio* clamped-nuclei eigenquantum-defect functions $\eta_{\ell\ell'}^{(\Lambda)}(R,\varepsilon)$ was carried out by adding an energy- and R-dependent correction function $c_{\ell\ell'}^{(\Lambda)}(R,\varepsilon)$. Each correction

function was constructed from six fit parameters defining the values of $c_{\ell\ell'}^{(\Lambda)}(R,\varepsilon)$ at the positions

$$(R/a_0, \varepsilon) = (2,0); (2, -1/4^2); (2, -1/3^2); (3,0); (3, -1/4^2); (3, -1/3^2). \tag{26}$$

The value of the correction function at arbitrary values of R and ε was obtained by extrapolation using a quadratic function along ε and a linear function along R.

In the fit of the negative-parity levels, a total of 12 fit parameters was adjusted and the set of experimental data consisted of 29 $n = 3$ energy levels,[38] 37 $n = 4$ energy levels,[30] and 107 energy levels with $4 < n < 20$ from the spectrum presented in Figure 3. Energy levels with $n \geq 20$ were not included in the fit because their energies are less sensitive to adjustments of the eigenquantum defects. In the subsequent fit of the positive-parity levels a total of 18 fit parameters was adjusted and the set of experimental data consisted of 21 $n = 2$ energy levels,[2,32] 68 $n = 3$ energy levels,[38] 36 $n = 4$ energy levels,[30] and 73 energy levels with $3 < n < 20$ from our new spectrum. The final values of the fit parameters are given in Table 5. As expected, the largest corrections of the eigenquantum defects are observed at $\varepsilon = 0$. The adjusted clamped-nuclei eigenquantum-defect curves at this energy for the $sd\Sigma, dd\Sigma$, and $dd\Delta$ symmetry are displayed as dash-dotted lines in panels (b), (c), and (e) of Figure 7, respectively. The adjusted eigenquantum defects for other energies and in the other panels are not shown, because they overlap with the corresponding *ab initio* curves on this scale. The adjusted clamped-nuclei eigenquantum-defect parameters are provided in Table 6. These parameters are mass-independent, *i.e.* they do not contain the corrections given in Eqs. (19) and (20), which must be added as appropriate for each isotopomer of molecular hydrogen.

To test the reliability of our adjustment procedure, we substantially varied the range over which the vibrational wavefunctions and eigenquantum-defect integrals of Eq. (10) were evaluated. For instance, by reducing $R_{\max}$ to $6\,a_0$ and using a vibrational basis $v_{\max}^+ = 15$ throughout, we found that the result of the fit remained unchanged. In this calculation the adjustments to the eigenquantum defects were made in the range from $R = 1.4\,a_0$ to $3.4\,a_0$ and the adjustment functions to the *ab initio* eigenquantum defects were represented as quadratic polynomials around $\varepsilon = 0$ and $R = 2.4\,a_0$.

The results of the MQDT calculations using the adjusted eigenquantum defects with the 'normal' and 'specific' mass corrections included are given in Tables 1, 3, and 4, and the calculated positions of all observed triplet ns and nd Rydberg states as well as predictions of so far unobserved Rydberg states with $n \leq 20$ are given in the Supporting Information. The agreement between calculated and observed energies is limited by the experimental resolution of $0.2\,\text{cm}^{-1}$ and the new set of MQDT parameters derived in the present work provides an accurate description of all triplet *gerade* Rydberg states of H_2 with $v^+ \leq 4$ observed to date. Our global fit reproduces 552 triplet *gerade* ns and nd levels of H_2, 361 of which have been measured in the present work, with a root-mean-square deviation of $0.2\,\text{cm}^{-1}$.

Conclusions

In the present investigation, new experimental data have been obtained on the triplet nd Rydberg states of H_2 in the range of principal quantum number $n = 5\text{–}45$ and vibrational quantum number $v^+ = 1\text{–}4$. Moreover, triplet ns Rydberg states of H_2 with $n > 4$ have been observed for the first time. The new data were combined with other spectroscopic data on $n \leq 4$ triplet *gerade* states available in the literature[2,30,32,38,39] to derive a global description of the triplet s and d ionization channels of H_2 by MQDT. Extrapolation of the observed Rydberg series to their limits and comparison with the known ionization energies of molecular hydrogen[25] has enabled the determination of the absolute energies of the triplet *gerade* Rydberg states and the metastable $c\,^3\Pi_\text{u}^-$ levels relative to the $X\,^1\Sigma_g^+\,(v = 0, N = 0)$ ground state of H_2. For the rovibrational levels of the $c\,^3\Pi_\text{u}^-$ state with ($v'' = 1\text{–}4, N'' = 1\text{–}3$) excellent agreement was found with the earlier measurements by Dieke[2,39] except for the ($v'' = 4, N'' = 2, 3$) levels, the term values of which were determined to be $103676.06(20)\,\text{cm}^{-1}$ and $103823.18(20)\,\text{cm}^{-1}$, respectively.

In the quantitative analysis of the triplet *gerade* Rydberg states of H_2 by MQDT, *ab initio* values of the energy- and R-dependent eigenquantum defects have been derived from the Born-Oppenheimer potential-energy curves of low-lying Rydberg states[62,62–65] and of the ground ionic

state.[66] For these low-lying Rydberg states ($n = 2$–4) the root-mean-square deviation between observed term values and term values calculated by *ab initio* MQDT was $0.5\,\mathrm{cm}^{-1}$. The deviations were larger for Rydberg states with $n = 5$–12, indicating that the energy-dependence of the eigenquantum defects is not linear.

The *ab initio* eigenquantum defects and their energy dependence up to the quadratic term were then refined in a global fit to the experimental data. The adjustments led to a reduction of the root-mean-square deviation to $0.2\,\mathrm{cm}^{-1}$ and to eigenquantum defects which are now known to a precision better than 0.005 in the range of internuclear distances from $1.6\,a_0$ to $3.7\,a_0$ and for energies corresponding to $n = 2$ up to the ionization continuum. In general, the s-d interaction parameters cannot be derived unambiguously from potential-energy curves.[17,18] Our analysis of experimental data and the assumption that all eigenquantum defects vary smoothly with the internuclear distance enabled us to overcome this ambiguity in the range of internuclear distances mentioned above. The adjusted eigenquantum defects and the experimental term values can serve as reference values for comparison with future *ab initio* calculations. The variational R-matrix approach has very recently been used[70] to compute triplet *gerade* η eigenquantum-defect matrices for H_2 from first principles in the range from $R = 1\,a_0$ to $5\,a_0$ and for energies from $n = 2$ up into the ionization continuum. Both singly and doubly excited electron-ion scattering channels were taken into account explicitly, and a procedure was developed to reduce these scattering parameters to eigenquantum defects equivalent to those extracted in the present work from molecular potential-energy curves and level positions obtained by high-resolution spectroscopy. Although the eigenquantum defects determined in the R-matrix calculations do not have the same accuracy as these determined in the present work, the R-matrix calculations remove all remaining conceptual ambiguities as to the physical meaning of the eigenquantum defects.[70]

Molecular hydrogen represents an ideal case for the study of perturbations in electronically excited states because both high-level *ab initio* calculations and accurate experimental data are available. Another molecule which has been studied at a comparable degree of detail is CaF, for which the initial values for the fit were determined by R-matrix calculations.[71] However, in that

example, unlike in the present work, it has not yet been possible to incorporate the lower states with $n - \delta \leq 4$ quantitatively in the global unified MQDT framework. In future, we plan to apply the same formalism to treat the singlet *gerade* states of molecular hydrogen and Rydberg states of molecular systems having more than two electrons.

Further, we stress that the highly accurate quantum-defect functions we have extracted here from a wealth of spectroscopic information on the triplet *gerade* states of H_2 have a meaning beyond the spectroscopic context considered here. Indeed, the physics of collisions involving ionization and dissociation processes of H_2 is governed by the same short-range physics as the Rydberg states studied here, that is, the same quantum-defect parameters – this has been demonstrated for triplet *gerade* symmetry in Refs. 49 and 39. Specifically, the present data should help to improve – and possibly revise – the assessment of the contribution of this symmetry to the dissociative recombination of H_2^+ ions with electrons.[72] Finally, the present work is also an example of how nonadiabatic dynamics in a large number of highly excited electronic states is amenable to an efficient and accurate quantum-mechanical treatment *via* frame-transformation theory. Tully, in a recent 'Perspective on non-adiabatic dynamics theory',[73] stated that 'nonadiabatic transitions between potential energy surfaces play a pivotal role in numerous chemical rate processes of current interest', but went on to caution that 'their treatment can be a formidable task that will require theoretical and computational advances that parallel the spectacular advances we are seeing in experimentation'. The present development might be viewed as a step in this direction.

Acknowledgement

Supporting Information Available

A list of all observed triplet *gerade* Rydberg states of H_2 and tables containing the results of MQDT calculations for triplet ns and nd Rydberg states with $n \leq 20$ are given in the Supporting Information. This material is available free of charge via the Internet at `http://pubs.acs.org/`.

References

(1) Richardson, O. W. *Molecular Hydrogen and its Spectrum*; Yale University Press: New Haven, 1934.

(2) Crosswhite, H. M. *The Hydrogen Molecule Wavelength Tables of Gerhard Heinrich Dieke*; Wiley-Interscience: New York, 1972.

(3) Chupka, W. A.; Berkowitz, J. *J. Chem. Phys.* **1969**, *51*, 4244–4268.

(4) Takezawa, S. *J. Chem. Phys.* **1970**, *52*, 2575–2590.

(5) Herzberg, G.; Jungen, Ch. *J. Mol. Spectrosc.* **1972**, *41*, 425–486.

(6) Dehmer, P. M.; Chupka, W. A. *J. Chem. Phys.* **1976**, *65*, 2243–2273.

(7) Glass-Maujean, M.; Jungen, Ch.; Schmoranzer, H.; Knie, A.; Haar, I.; Hentges, R.; Kielich, W.; Jänkälä, K.; Ehresmann, A. *Phys. Rev. Lett.* **2010**, *104*, 183002.

(8) Glass-Maujean, M.; Jungen, Ch.; Reichardt, G.; Balzer, A.; Schmoranzer, H.; Ehresmann, A.; Haar, I.; Reiss, P. *Phys. Rev. A* **2010**, *82*, 062511.

(9) Jungen, Ch.; Atabek, O. *J. Chem. Phys.* **1977**, *66*, 5584–5609.

(10) Jungen, Ch.; Raoult, M. *Faraday Discuss.* **1981**, *71*, 253–271.

(11) Glass-Maujean, M.; Jungen, Ch.; Roudjane, M.; Tchang-Brillet, W.-Ü. L. *J. Chem. Phys.* **2011**, *134*, 204305.

(12) Sprecher, D.; Jungen, Ch.; Ubachs, W.; Merkt, F. *Faraday Discuss.* **2011**, *150*, 51 –70.

(13) Quadrelli, P.; Dressler, K.; Wolniewicz, L. *J. Chem. Phys.* **1990**, *93*, 4958–4964.

(14) Wolniewicz, L.; Dressler, K. *J. Chem. Phys.* **1994**, *100*, 444–451.

(15) Yu, S.; Dressler, K. *J. Chem. Phys.* **1994**, *101*, 7692.

(16) Ross, S.; Jungen, Ch. *Phys. Rev. Lett.* **1987**, *59*, 1297–1300.

(17) Ross, S. C.; Jungen, Ch. *Phys. Rev. A* **1994**, *49*, 4353–4363.

(18) Ross, S. C.; Jungen, Ch. *Phys. Rev. A* **1994**, *49*, 4364–4377.

(19) Ross, S. C.; Jungen, Ch. *Phys. Rev. A* **1994**, *50*, 4618–4628.

(20) Ross, S. C.; Yoshinari, T.; Ogi, Y.; Tsukiyama, K. *J. Chem. Phys.* **2006**, *125*, 133205.

(21) Rottke, H.; Welge, K. H. *J. Chem. Phys.* **1992**, *97*, 908–926.

(22) Glab, W. L.; Qin, K.; Bistransin, M. *J. Chem. Phys.* **1995**, *102*, 2338–2350.

(23) Osterwalder, A.; Seiler, R.; Merkt, F. *J. Chem. Phys.* **2000**, *113*, 7939–7944.

(24) Osterwalder, A.; Wüest, A.; Merkt, F.; Jungen, Ch. *J. Chem. Phys.* **2004**, *121*, 11810–11838.

(25) Liu, J.; Salumbides, E. J.; Hollenstein, U.; Koelemeij, J. C. J.; Eikema, K. S. E.; Ubachs, W.; Merkt, F. *J. Chem. Phys.* **2009**, *130*, 174306.

(26) Liu, J.; Sprecher, D.; Jungen, Ch.; Ubachs, W.; Merkt, F. *J. Chem. Phys.* **2010**, *132*, 154301.

(27) Sprecher, D.; Liu, J.; Jungen, Ch.; Ubachs, W.; Merkt, F. *J. Chem. Phys.* **2010**, *133*, 111102.

(28) Lichten, W.; Wik, T.; Miller, T. A. *J. Chem. Phys.* **1979**, *71*, 2441–2457.

(29) Eyler, E. E.; Pipkin, F. M. *J. Chem. Phys.* **1982**, *77*, 5315–5318.

(30) Eyler, E. E.; Pipkin, F. M. *Phys. Rev. A* **1983**, *27*, 2462–2478.

(31) Koot, W.; van der Zande, W. J.; Los, J.; Keiding, S. R.; Bjerre, N. *Phys. Rev. A* **1989**, *39*, 590–604.

(32) Jungen, Ch.; Dabrowski, I.; Herzberg, G.; Vervloet, M. *J. Chem. Phys.* **1990**, *93*, 2289–2298.

(33) Alikacem, A.; Larzillière, M. *J. Chem. Phys.* **1990**, *93*, 215–223.

(34) Jozefowski, L.; Ottinger, Ch.; Rox, T. *J. Mol. Spectrosc.* **1994**, *163*, 381–397.

(35) Jozefowski, L.; Ottinger, Ch.; Rox, T. *J. Mol. Spectrosc.* **1994**, *163*, 398–413.

(36) Ottinger, Ch.; Rox, T.; Sharma, A. *J. Mol. Spectrosc.* **1994**, *163*, 414–427.

(37) Uy, D.; Gabrys, C. M.; Oka, T.; Cotterell, B. J.; Stickland, R. J.; Jungen, Ch.; Wüest, A. *J. Chem. Phys.* **2000**, *113*, 10143–10153.

(38) Bailly, D.; Vervloet, M. *Mol. Phys.* **2007**, *105*, 1559–1564.

(39) Ross, S. C.; Jungen, Ch.; Matzkin, A. *Can. J. Phys.* **2001**, *79*, 561–588.

(40) Knight, R. D.; Wang, L.-G. *Phys. Rev. Lett.* **1985**, *55*, 1571–1574.

(41) Kachru, R.; Helm, H. *Phys. Rev. Lett.* **1985**, *55*, 1575–1578.

(42) Harries, J. R.; Hammond, P.; Chandler, R.; Murray, A. J. *J. Phys. B: At. Mol. Opt. Phys.* **2004**, *37*, 179–199.

(43) Dinu, L.; Picard, Y. J.; van der Zande, W. J. *J. Chem. Phys.* **2004**, *121*, 3058–3068.

(44) de Bruijn, D. P.; Helm, H. *Phys. Rev. A* **1986**, *34*, 3855–3864.

(45) Bjerre, N.; Keiding, S. R.; Lembo, L. J.; Helm, H. *Phys. Rev. Lett.* **1988**, *60*, 2465–2468.

(46) Lembo, L. J.; Huestis, D. L.; Keiding, S. R.; Bjerre, N.; Helm, H. *Phys. Rev. A* **1988**, *38*, 3447–3455.

(47) Lembo, L. J.; Bjerre, N.; Huestis, D. L.; Helm, H. *J. Chem. Phys.* **1990**, *92*, 2219–2228.

(48) Siebbeles, L. D. A.; Schins, J. M.; Los, J.; Glass-Maujean, M. *Phys. Rev. A* **1991**, *44*, 1584–1596.

(49) Matzkin, A.; Jungen, Ch.; Ross, S. C. *Phys. Rev. A* **2000**, *62*, 062511.

(50) Halfmann, T.; Koensgen, J.; Bergmann, K. *Meas. Sci. Technol.* **2000**, *11*, 1510–1514.

(51) Wiederkehr, A. W.; Motsch, M.; Hogan, S. D.; Andrist, M.; Schmutz, H.; Lambillotte, B.; Agner, J. A.; Merkt, F. *J. Chem. Phys.* **2011**, *135*, 214202.

(52) Korobov, V. I. *Phys. Rev. A* **2008**, *77*, 022509.

(53) Moss, R. E. *Mol. Phys.* **1993**, *80*, 1541–1554.

(54) Berg, Ch.; Ottinger, Ch. *J. Chem. Phys.* **1994**, *100*, 8746–8754.

(55) Jungen, Ch.; Miescher, E. *Can. J. Phys.* **1969**, *47*, 1769–1787.

(56) Lichten, W.; Wik, T. *J. Chem. Phys.* **1978**, *69*, 5428–5437.

(57) Greene, C. H.; Jungen, Ch. *Adv. At. Mol. Phys.* **1985**, *21*, 51–121.

(58) Jungen, Ch. *Elements of Quantum Defect Theory* in *Handbook of High-resolution Spectroscopy*; Quack, M., Merkt, F., Eds.; John Wiley & Sons, Ltd., 2011.

(59) Guérout, R.; Jungen, Ch.; Oueslati, H.; Ross, S. C.; Telmini, M. *Phys. Rev. A* **2009**, *79*, 042717.

(60) Du, N. Y.; Greene, C. H. *J. Chem. Phys.* **1986**, *85*, 5430–5436.

(61) Jungen, Ch.; Raseev, G. *Phys. Rev. A* **1998**, *57*, 2407–2419.

(62) Staszewska, G.; Wolniewicz, L. *J. Mol. Spectrosc.* **1999**, *198*, 416–420.

(63) Kołos, W.; Rychlewski, J. *J. Mol. Spectrosc.* **1996**, *177*, 146–153.

(64) Staszewska, G. *J. Phys. Chem. A* **2001**, *105*, 2308–2311.

(65) Wolniewicz, L. *J. Mol. Spectrosc.* **1995**, *174*, 132–136.

(66) Bishop, D. M.; Wetmore, R. W. *Mol. Phys.* **1973**, *26*, 145–157.

(67) Kołos, W.; Rychlewski, J. *J. Mol. Spectrosc.* **1995**, *169*, 341–351.

(68) Wolniewicz, L. (private communication).

(69) Greene, C. H.; Jungen, Ch. *Phys. Rev. Lett.* **1985**, *55*, 1066–1069.

(70) Oueslati, H.; Argoubi, F.; Telmini, M.; Sprecher, D.; Jungen, Ch. (in preparation).

(71) Kay, J. J.; Coy, S. L.; Wong, B. M.; Jungen, Ch.; Field, R. W. *J. Chem. Phys.* **2011**, *134*, 114313.

(72) Florescu, A. I.; Ngassam, V.; Schneider, I. F.; Suzor-Weiner, A. *J. Phys. B* **2003**, *36*, 1205.

(73) Tully, J. C. *J. Chem. Phys.* **2012**, *137*, 22A301, and following articles in the same issue.

Table 1: Observed term values $\tilde{\nu}_{\text{obs}}$ and effective quantum defects δ of the $n\text{d}1_N\,(1)$ Rydberg series with $n \le 30$. The uncertainty of $\tilde{\nu}_{\text{obs}}$ is $0.2\,\text{cm}^{-1}$ and gives rise to uncertainties of δ given in brackets in units of the last digit. The results of the MQDT calculations using *ab initio* ($\tilde{\nu}_{\text{abi}}$) and adjusted ($\tilde{\nu}_{\text{adj}}$) eigenquantum defects are given relative to the observed values. All values are in units of cm^{-1} except n and δ which are unitless. A table containing all observed ns and nd Rydberg states is provided as Supporting Information.

| n | $n\text{d}1_1\,(v^+ = 1)$ Rydberg series | | | | $n\text{d}1_2\,(v^+ = 1)$ Rydberg series | | | |
	$\tilde{\nu}_{\text{obs}}$	δ	$\tilde{\nu}_{\text{abi}} - \tilde{\nu}_{\text{obs}}$	$\tilde{\nu}_{\text{adj}} - \tilde{\nu}_{\text{obs}}$	$\tilde{\nu}_{\text{obs}}$	δ	$\tilde{\nu}_{\text{abi}} - \tilde{\nu}_{\text{obs}}$	$\tilde{\nu}_{\text{adj}} - \tilde{\nu}_{\text{obs}}$
10	125547.01	0.089(1)	2.72	−0.00	125561.75	0.023(1)	−0.79	−0.25
11	obscured				125757.28	−0.001(1)	−0.93	−0.05
12	125893.63	0.065(2)	0.57	−0.13	125902.99	−0.008(2)	−0.83	−0.00
13	126007.54	0.070(2)	0.82	−0.13	126013.83	0.008(2)	−0.48	−0.04
14	126098.64	0.067(3)	0.43	−0.07	126104.29	−0.003(3)	−0.50	−0.01
15	126172.21	0.061(3)	0.04	−0.05	126177.29	−0.017(3)	−0.51	0.02
16	126231.61	0.067(4)	0.25	−0.09	126235.37	−0.002(4)	−0.34	0.01
17	obscured				126286.14	−0.044(4)	−0.44	−0.01
18	126322.58	0.069(5)	0.19	−0.05	126325.31	−0.003(5)	−0.25	−0.00
19	obscured				126359.87	0.001(6)	−0.22	−0.02
20	126387.57	0.071(7)	0.11	−0.04	126389.70	−0.007(7)	−0.21	−0.01
21	obscured				126415.09	−0.003(8)	−0.18	−0.02
22	obscured				126437.13	−0.001(10)	−0.18	−0.06
23	126455.53	0.048(11)	0.01	−0.10	126456.60	−0.011(11)	−0.20	−0.06
24	126472.40	0.058(13)	−0.01	−0.07	126473.43	−0.007(13)	−0.17	−0.06
25	126487.48	0.055(14)	0.02	−0.11	126488.33	−0.005(14)	−0.14	−0.06
26	126500.75	0.060(16)	0.04	−0.10	126501.51	−0.001(16)	−0.15	−0.08
27	126512.69	0.054(18)	−0.03	−0.10	126513.45	−0.014(18)	−0.15	−0.06
28	126523.31	0.054(20)	−0.04	−0.11	126523.97	−0.012(20)	−0.15	−0.08
29	126532.85	0.054(22)	−0.04	−0.11	126533.44	−0.011(22)	−0.14	−0.08
30	126541.45	0.054(25)	−0.04	−0.11	126541.98	−0.011(25)	−0.14	−0.08

Table 2: List of Hund's-case-(b) and Hund's-case-(d) channels which contribute to a state with given parity and N value.

Electronic parity	N	contributing channels	
		Hund's case (b)[a]	Hund's case (d)[b]
+	0	$n\mathrm{s}\Sigma_g^+,\ n\mathrm{d}\Sigma_g^+$	$n\mathrm{s}0_0,\ n\mathrm{d}2_0$
	1	$n\mathrm{s}\Sigma_g^+,\ n\mathrm{d}\Sigma_g^+,\ n\mathrm{d}\Pi_g^+$	$n\mathrm{s}1_1,\ n\mathrm{d}1_1,\ n\mathrm{d}3_1$
	≥ 2	$n\mathrm{s}\Sigma_g^+,\ n\mathrm{d}\Sigma_g^+,$	$n\mathrm{s}(N)_N,\ n\mathrm{d}(N)_N,$
		$n\mathrm{d}\Pi_g^+,\ n\mathrm{d}\Delta_g^+$	$n\mathrm{d}(N\pm2)_N$
−	1	$n\mathrm{d}\Pi_g^-$	$n\mathrm{d}2_1$
	≥ 2	$n\mathrm{d}\Pi_g^-,\ n\mathrm{d}\Delta_g^-$	$n\mathrm{d}(N\pm1)_N$

[a]Notation: $n\ell\,\Lambda_{g/u}^{\pm}$
[b]Notation: $n\ell(N^+)_N$

Table 3: Literature values of observed term values $\tilde{\nu}_{\mathrm{obs}}$ for $N = 2$ states with $n = 2$ (from Refs. 2 and 32), $n = 3$ (from Ref. 38), and $n = 4$ (from Refs. 30 and 39). The results of the MQDT calculations using *ab initio* ($\tilde{\nu}_{\mathrm{abi}}$) and adjusted ($\tilde{\nu}_{\mathrm{adj}}$) eigenquantum defects are given relative to the observed values. All values are in units of cm^{-1}. A table containing term values calculated by MQDT for other N values is provided as Supporting Information.

Label	v	$\tilde{\nu}_{\mathrm{obs}}$	$\tilde{\nu}_{\mathrm{abi}} - \tilde{\nu}_{\mathrm{obs}}$	$\tilde{\nu}_{\mathrm{adj}} - \tilde{\nu}_{\mathrm{obs}}$	Label	v	$\tilde{\nu}_{\mathrm{obs}}$	$\tilde{\nu}_{\mathrm{abi}} - \tilde{\nu}_{\mathrm{obs}}$	$\tilde{\nu}_{\mathrm{adj}} - \tilde{\nu}_{\mathrm{obs}}$
\multicolumn{5}{c}{$n = 2$, positive electronic parity}	\multicolumn{5}{c}{$n = 4$, positive electronic parity}
$a\,^3\Sigma_g^+$	0	95275.79	0.44	0.02	$4d\,^3\Sigma_g^+$	0	117417.64	0.61	0.10
$a\,^3\Sigma_g^+$	1	97790.35	0.14	−0.05	$4s\,^3\Sigma_g^+$	0	117609.61	0.45	0.04
$a\,^3\Sigma_g^+$	2	100169.19	−0.21	−0.09	$4d\,^3\Pi_g^+$	0	117718.98	0.33	0.35
\multicolumn{5}{c}{$n = 3$, positive electronic parity}	$4d\,^3\Delta_g^+$	0	117958.40	0.47	−0.08
$g\,^3\Sigma_g^+$	0	111826.48	−0.25	−0.05	$4d\,^3\Sigma_g^+$	1	119566.73	0.59	−0.03
$h\,^3\Sigma_g^+$	0	112049.97	0.06	−0.01	$4s\,^3\Sigma_g^+$	1	119823.00	0.37	−0.03
$i\,^3\Pi_g^+$	0	112310.88	−0.13	0.19	$4d\,^3\Pi_g^+$	1	119897.32	0.28	0.07
$j\,^3\Delta_g^+$	0	112529.55	−0.26	0.15	$4d\,^3\Delta_g^+$	1	120086.37	0.18	−0.28
$g\,^3\Sigma_g^+$	1	113910.92	−0.91	−0.16	$4s\,^3\Sigma_g^+$	2	121904.91	0.26	−0.06
$h\,^3\Sigma_g^+$	1	114312.07	0.09	−0.09	$4d\,^3\Pi_g^+$	2	121951.60	0.46	−0.01
$i\,^3\Pi_g^+$	1	114419.34	−0.61	−0.01	$4d\,^3\Delta_g^+$	2	122093.78	−0.02	−0.18
$j\,^3\Delta_g^+$	1	114711.99	−0.21	0.25	$n = 4$, negative electronic parity
$g\,^3\Sigma_g^+$	2	115829.39	−1.87	−0.13	$4d\,^3\Pi_g^-$	0	117599.44	0.17	0.00
$i\,^3\Pi_g^+$	2	116319.26	−0.99	0.05	$4d\,^3\Delta_g^-$	0	117830.35	−0.10	−0.17
$h\,^3\Sigma_g^+$	2	116501.86	−0.09	−0.16	$4d\,^3\Pi_g^-$	1	119770.24	−0.05	−0.09
$j\,^3\Delta_g^+$	2	116777.88	−0.21	0.22	$4d\,^3\Delta_g^-$	1	119997.24	−0.41	−0.24
\multicolumn{5}{c}{$n = 3$, negative electronic parity}	$4d\,^3\Pi_g^-$	2	121802.95	−0.21	−0.07
$i\,^3\Pi_g^-$	0	112140.80	−0.01	−0.25	$4d\,^3\Delta_g^-$	2	122042.65	−0.38	−0.09
$j\,^3\Delta_g^-$	0	112513.90	−0.17	0.28	$4d\,^3\Pi_g^-$	3	123696.11	−0.69	−0.17
$i\,^3\Pi_g^-$	1	114258.96	−0.36	−0.17	$4d\,^3\Delta_g^-$	3	123969.04	−0.36	0.05
$j\,^3\Delta_g^-$	1	114706.70	−0.23	0.22					
$i\,^3\Pi_g^-$	2	116227.87	−1.02	−0.20					
$j\,^3\Delta_g^-$	2	116776.12	−0.18	0.23					

Table 4: Assignment of the lines labeled by the letters A–P in Figs. 6 and 9. $\tilde{v}_{\text{obs}}$ **is the term value of the corresponding final Rydberg state (uncertainty** $0.2\,\text{cm}^{-1}$**). The results of the MQDT calculations using *ab initio* (**$\tilde{v}_{\text{abi}}$**) and adjusted (**$\tilde{v}_{\text{adj}}$**) eigenquantum defects are given relative to the observed values. All values are in units of** cm^{-1}**. A table containing all observed** n**s and** n**d Rydberg states is provided as Supporting Information.**

Observed transition[a]	$\tilde{v}_{\text{obs}}$	$\tilde{v}_{\text{abi}} - \tilde{v}_{\text{obs}}$	$\tilde{v}_{\text{adj}} - \tilde{v}_{\text{obs}}$
A: $7d1_1\,(5) \leftarrow (4,1)$	131847.02	2.17	0.25
B: $9d3_1\,(1) \leftarrow (1,1)$	125562.69	1.07	−0.29
C: $9d3_2\,(1) \leftarrow (1,1)$	125576.44	−1.45	−0.17
D: $6d3_2\,(3) \leftarrow (2,1)$	127799.29	−2.06	−0.17
E: $11d0_2\,(1) \leftarrow (1,2)$	125698.83	−0.64	−0.11
F: $6d1_1\,(2) \leftarrow (1,1)$	125594.09	3.31	−0.15
G: $6d2_1\,(2) \leftarrow (1,2)$	125716.14	−0.59	0.23
H: $6d3_2\,(2) \leftarrow (1,3)$	125890.12	−1.44	0.10
I: $6d3_4\,(2) \leftarrow (1,3)$	125925.70	−2.32	0.14
J: $6s1_1\,(2) \leftarrow (1,1)$	125642.00	0.71	0.11
K: $6d2_2\,(1) \leftarrow (1,2)$	125760.15	−0.21	0.21
L: $12d3_2\,(4) \leftarrow (4,1)$	131948.06	−1.42	−0.04
M: $6d2_3\,(2) \leftarrow (1,2)$	125770.89	−2.08	0.10
N: $10d3_2\,(2) \leftarrow (2,1)$	127877.34	−0.73	−0.16
O: $6d1_2\,(2) \leftarrow (1,1)$	125675.62	−2.60	0.01
P: $5d1_1\,(4) \leftarrow (2,1)$	127893.81	3.93	−0.27

[a]Notation: $n\ell N_N^+(v^+) \leftarrow (v'', N'')$

Table 5: Final values of the fit parameters $c_{\ell\ell'}^{(\Lambda)}(R,\varepsilon)$ in units of 10^{-4} [see Eq. (26) and preceding text]. The standard deviation in units of the last digit is given in parentheses.

	$\varepsilon = 0^a$	$\varepsilon = -1/4^2$	$\varepsilon = -1/3^2$
Fit to levels with negative electronic parity			
dd Π, $R = 2$	$-17(4)$	$2.6(6)$	$1.9(3)$
dd Π, $R = 3$	$-29(6)$	$-5.8(10)$	$-4.5(7)$
dd Δ, $R = 2$	$-76(6)$	$-1.0(8)$	$-2.0(4)$
dd Δ, $R = 3$	$-124(8)$	$-0.8(18)$	$-2.1(14)$
Fit to levels with positive electronic parity			
ss Σ, $R = 2$	$3(1)$	$1.3(3)$	$0.4(1)$
ss Σ, $R = 3$	$5(4)$	$3.1(12)$	$1.8(7)$
sd Σ, $R = 2$	$29(8)$	$1.5(10)$	$-0.6(3)$
sd Σ, $R = 3$	$28(8)$	$0.0(22)$	$-0.8(8)$
dd Σ, $R = 2$	$228(6)$	$5.4(8)$	$-6.9(3)$
dd Σ, $R = 3$	$190(4)$	$16.8(19)$	$-12.6(7)$

[a]The values at $\varepsilon = 0$ originate from an extrapolation and the actual uncertainty is expected to be larger than the standard deviation.

Table 6: Taylor coefficients $\frac{\partial^k \eta_{\ell\ell'}^{(\Lambda)}(R,\varepsilon=0)}{\partial \varepsilon^k}$ of the adjusted clamped-nuclei eigenquantum defects [see Eq. (23)] and the isotope-independent specific-mass correction $\frac{\mu}{m}\Delta_{\mathrm{sm}}\eta_{\mathrm{ss}}^{(\Sigma)}(R)$ [see Eq. (20)].

R/a_0	$\eta_{\mathrm{ss}}^{(\Sigma)}$	$\frac{\partial\eta_{\mathrm{ss}}^{(\Sigma)}}{\partial\varepsilon}$	$\frac{\partial^2\eta_{\mathrm{ss}}^{(\Sigma)}}{\partial\varepsilon^2}$	$\eta_{\mathrm{sd}}^{(\Sigma)}$	$\frac{\partial\eta_{\mathrm{sd}}^{(\Sigma)}}{\partial\varepsilon}$	$\frac{\partial^2\eta_{\mathrm{sd}}^{(\Sigma)}}{\partial\varepsilon^2}$	$\eta_{\mathrm{dd}}^{(\Sigma)}$	$\frac{\partial\eta_{\mathrm{dd}}^{(\Sigma)}}{\partial\varepsilon}$	$\frac{\partial^2\eta_{\mathrm{dd}}^{(\Sigma)}}{\partial\varepsilon^2}$
1.0	0.1653394	−0.071669	−0.01684	0.0005072	0.067181	0.66857	0.0365975	0.497851	7.98720
1.2	0.1381253	−0.073770	0.00506	−0.0006260	0.068708	0.67911	0.0414362	0.416957	7.57616
1.4	0.1114428	−0.076379	0.02737	−0.0019612	0.070432	0.68965	0.0470129	0.320858	7.16787
1.6	0.0856467	−0.080435	0.04559	−0.0034983	0.072356	0.70018	0.0531777	0.206551	6.76041
1.8	0.0609229	−0.085891	0.05988	−0.0052374	0.074478	0.71072	0.0609624	0.081447	6.35296
2.0	0.0371897	−0.093730	0.06469	−0.0071785	0.076798	0.72126	0.0705695	−0.054047	5.94550
2.2	0.0146357	−0.101428	0.07322	−0.0093216	0.079318	0.73180	0.0824451	−0.196741	5.53805
2.4	−0.0068447	−0.110452	0.07732	−0.0116666	0.082035	0.74234	0.0973862	−0.338618	5.13059
2.6	−0.0272181	−0.120736	0.07662	−0.0142137	0.084952	0.75288	0.1161701	−0.469719	4.72314
2.8	−0.0464500	−0.132447	0.06893	−0.0169627	0.088067	0.76341	0.1395867	−0.577380	4.31568
3.0	−0.0644725	−0.145674	0.05178	−0.0199137	0.091380	0.77395	0.1681802	−0.648760	3.90823
3.2	−0.0811780	−0.160348	0.02268	−0.0230666	0.094892	0.78449	0.2019295	−0.674727	3.50077
3.4	−0.0963993	−0.175968	−0.01884	−0.0264216	0.098603	0.79503	0.2400292	−0.653368	3.09332
3.6	−0.1098795	−0.191207	−0.06875	−0.0299786	0.102512	0.80557	0.2809343	−0.591043	2.68586
3.8	−0.1212217	−0.203156	−0.11409	−0.0337375	0.106620	0.81610	0.3227333	−0.499873	2.27840
4.0	−0.1298032	−0.206232	−0.12752	−0.0376984	0.110926	0.82664	0.3636694	−0.393260	1.87095
4.2	−0.1260103	−0.068723	0.67376	−0.0418612	0.115431	0.83718	0.4025801	−0.281885	1.46349
4.4	−0.1239069	0.007588	1.06610	−0.0462261	0.120135	0.84772	0.4389853	−0.172070	1.05604
4.6	−0.1406495	−0.225331	−0.47032	−0.0507929	0.125037	0.85826	0.4731135	−0.065539	0.64858
4.8	−0.1339258	−0.173946	−0.37200	−0.0555617	0.130138	0.86880	0.5060093	0.040386	0.24113
5.0	−0.0004046	1.612248	10.05682	−0.0605324	0.135437	0.87933	0.5391717	0.150114	−0.16633

| R/a_0	$\eta_{\mathrm{dd}}^{(\Pi)}$	$\frac{\partial\eta_{\mathrm{dd}}^{(\Pi)}}{\partial\varepsilon}$	$\frac{\partial^2\eta_{\mathrm{dd}}^{(\Pi)}}{\partial\varepsilon^2}$	$\eta_{\mathrm{dd}}^{(\Delta)}$	$\frac{\partial\eta_{\mathrm{dd}}^{(\Delta)}}{\partial\varepsilon}$	$\frac{\partial^2\eta_{\mathrm{dd}}^{(\Delta)}}{\partial\varepsilon^2}$	$\frac{\mu}{m}\Delta_{\mathrm{sm}}\eta_{\mathrm{ss}}^{(\Sigma)}$
1.0	0.0126893	−0.064155	0.44565	−0.0017452	−0.024897	−0.78804	−0.013357
1.2	0.0166888	−0.071862	0.80990	−0.0035694	−0.020500	−1.06833	−0.014421
1.4	0.0214629	−0.081730	1.23597	−0.0056579	−0.011928	−1.34862	−0.015530
1.6	0.0271177	−0.092833	1.74148	−0.0079848	0.000403	−1.62890	−0.016734
1.8	0.0336413	−0.107771	2.30718	−0.0105342	0.015892	−1.90919	−0.017971
2.0	0.0412855	−0.123682	2.97387	−0.0132705	0.034043	−2.18948	−0.019273
2.2	0.0501762	−0.144132	3.69255	−0.0162326	0.053640	−2.46977	−0.020667
2.4	0.0608984	−0.162887	4.52599	−0.0193566	0.074257	−2.75006	−0.021682
2.6	0.0734623	−0.191924	5.31684	−0.0226103	0.095179	−3.03034	−0.023748
2.8	0.0890642	−0.222636	6.09463	−0.0260112	0.115293	−3.31063	−0.025472
3.0	0.1094968	−0.244921	6.83306	−0.0295314	0.133761	−3.59092	−0.027294
3.2	0.1384165	−0.225801	7.62431	−0.0331401	0.149779	−3.87121	−0.029322
3.4	0.1844983	−0.050237	9.21164	−0.0368004	0.162630	−4.15150	−0.031438
3.6	0.2690947	0.631118	14.40926	−0.0404742	0.171625	−4.43178	−0.033741
3.8	0.4377318	2.626436	30.08118	−0.0441250	0.176109	−4.71207	−0.036208
4.0	0.7322140	6.587200	60.71949	−0.0477176	0.175465	−4.99236	−0.038755
4.2	1.0708810	10.758304	88.75324	−0.0512158	0.169123	−5.27265	−0.040885
4.4	1.3240624	13.011334	97.69199	−0.0545792	0.156704	−5.55294	−0.043294
4.6	1.4802308	13.666861	94.12759	−0.0577669	0.137880	−5.83322	−0.047122
4.8	1.5927680	13.870892	88.77683	−0.0607400	0.112477	−6.11351	−0.049735
5.0	1.7150227	14.477639	87.79355	−0.0634621	0.080473	−6.39380	−0.043659
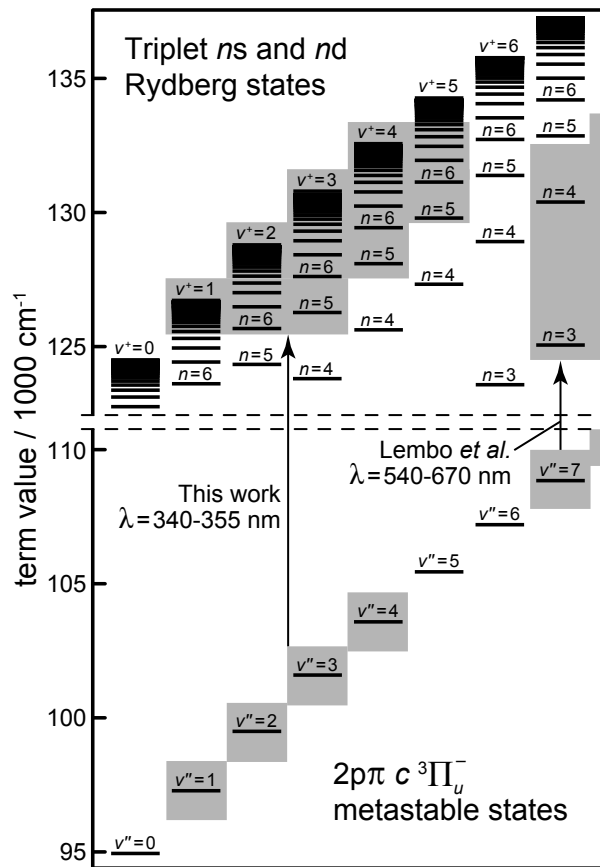
Figure 1: Energy-level diagram of the metastable states and the triplet *n*s and *n*d Rydberg states of H_2. Only states with rotational quantum number 1 are shown for clarity. The gray areas connected by arrows designate initial and final states observed in this work (left) and by Lembo *et al.*[47] (right).
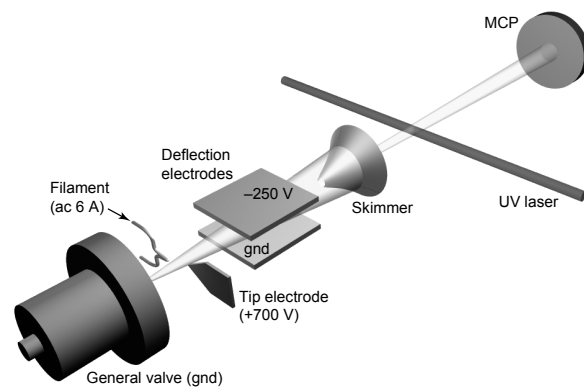
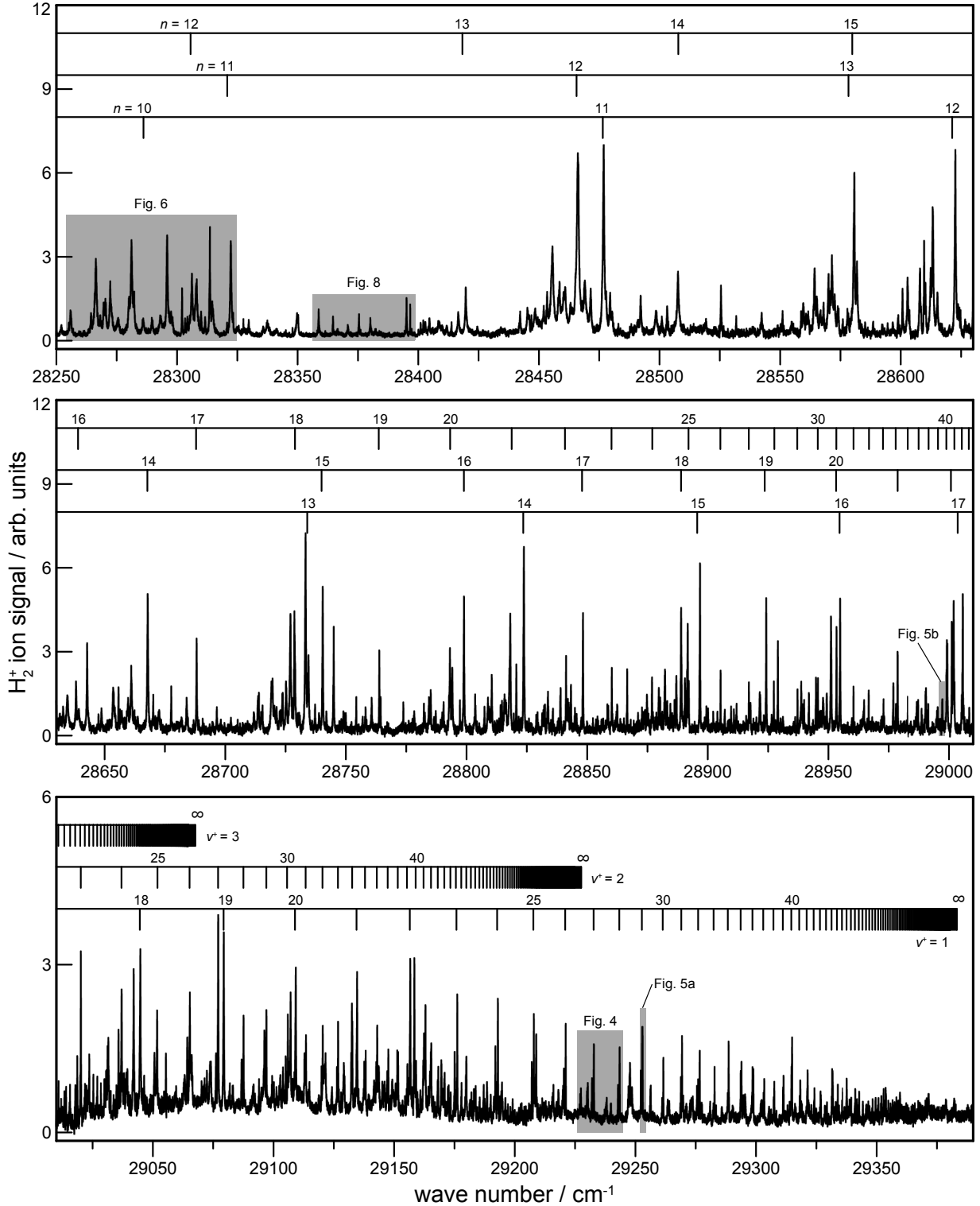Figure 2: Schematic representation of the experimental configuration (see text for details).

Figure 3: Overview of the observed spectrum of the $n\ell N_N^+(v^+) \leftarrow c\,^3\Pi_u^-(v'',N'')$ band system of H_2. The assignment bars indicate the approximate positions of the transitions $n\mathrm{d}1_{1,2}(v^+) \leftarrow (v'',1)$ with $v^+ = v'' = 1$ (lowest assignment bar), $v^+ = v'' = 2$ (central assignment bar), and $v^+ = v'' = 3$ (highest assignment bar). The gray regions are depicted on a enlarged scale in the specified figures.
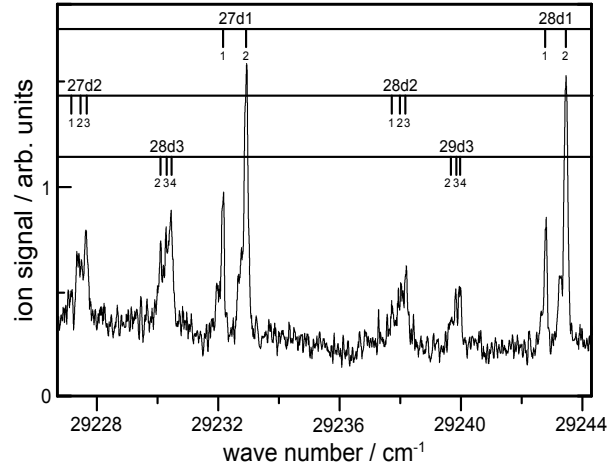
Figure 4: Enlarged view of the $ndN_N^+(v^+ = 1) \leftarrow c^3\Pi_u^-(v'' = 1, N'')$ transitions of H_2 near $n =$ 27. The assignment bars indicate the positions of the transitions with $N^+ = N'' = 1$ (top), $N^+ = N'' = 2$ (middle), and $N^+ = N'' = 3$ (bottom). The orbital fine structure is also indicated and the corresponding N values are given below the assignment bars.
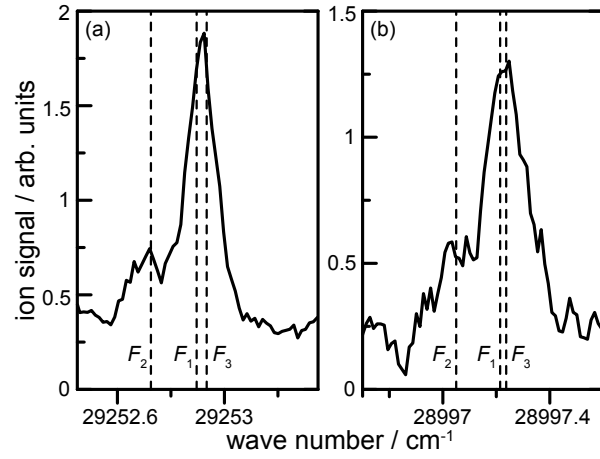
Figure 5: Enlarged view of the (a) $29d1_2(1) \leftarrow (1,1)$ and (b) $17d2_2(1) \leftarrow (1,2)$ transitions. The vertical dashed lines indicate the expected splittings resulting from the spin fine structure of the metastable state.
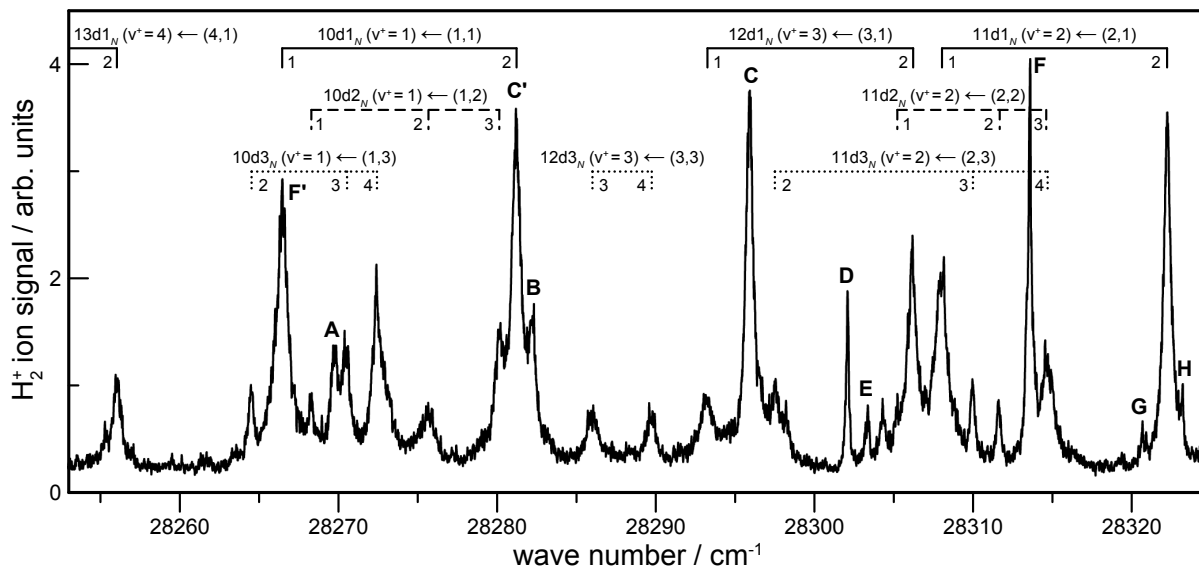
Figure 6: Enlarged view of the observed spectrum in the region of the $10d1_2(1) \leftarrow (1,1)$ transition. The assignment bars indicate the positions of the transitions with $v^+ = v''$ and $N^+ = N'' = 1$ (full), $N^+ = N'' = 2$ (dashed), and $N^+ = N'' = 3$ (dotted). The N values of different orbital fine components are given next to each assignment bar. The letters **A**–**H** label transitions to rotational and vibrational perturbers ($v^+ \neq v''$ and/or $N^+ \neq N''$) and their assignments are given in Table 4.
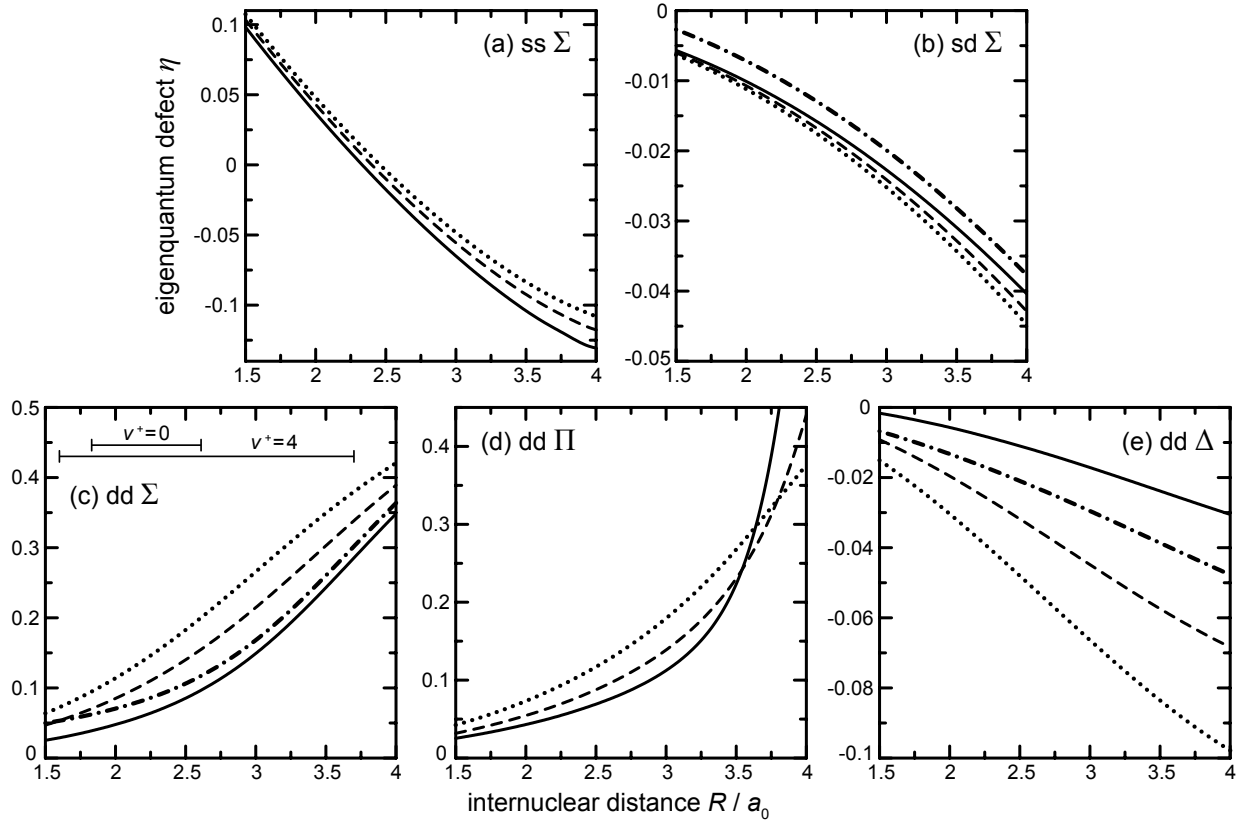
Figure 7: Panels (a)–(e) contain diagrams of the clamped-nuclei eigenquantum-defect parameters $\eta_{\ell\ell'}^{(\Lambda)}$ for the specified values of ℓ, ℓ', and Λ. The solid, dashed, and dotted lines depict the *ab initio* eigenquantum defects for $\varepsilon = 0, -1/4^2$, and $-1/3^2$, respectively. The dash-dotted lines in panels (b), (c), and (e), represent the eigenquantum defects for $\varepsilon = 0$ after adjustment to experimental data. The intervals given at the top of panel (c) depict the range of R for which the probability density of H_2^+ in the states $(v^+ = 0, N^+ = 0)$ and $(v^+ = 4, N^+ = 0)$ is 95 %.
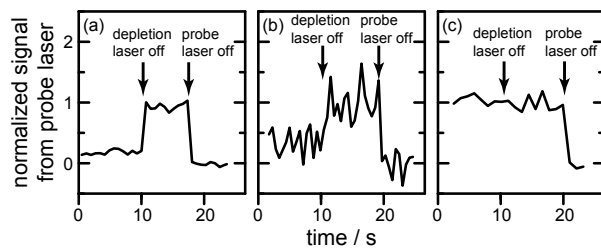
Figure 8: Three representative traces recorded using the double-resonance technique. The depletion laser was fixed on the **C**: $9d3_2(1) \leftarrow (1,1)$ transition and the probe laser was tuned to (a) the **B**: $9d3_1(1) \leftarrow (1,1)$, (b) the **J**: $6s1_1(1) \leftarrow (1,1)$, and (c) the **M**: $6d2_3(2) \leftarrow (1,2)$ transition.
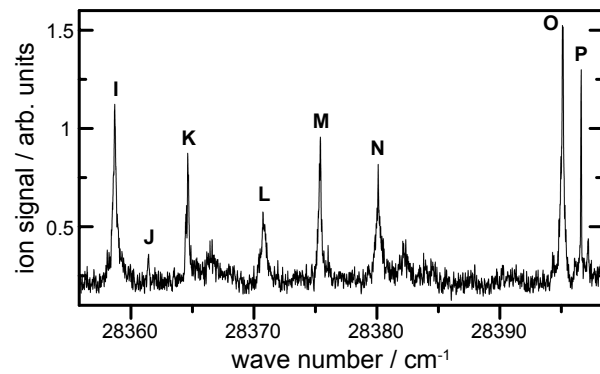
Figure 9: Enlarged view of the observed spectrum in the region of the $6s1_1(1) \leftarrow (1,1)$ transition (label **J**). The assignments of the lines labeled by letters **I–P** are given in Table 4.

Graphical TOC Entry